Reaction-Path Energetics and Kinetics of the Hydride Transfer Reaction Catalyzed by Dihydrofolate Reductase†

Mireia Garcia-Viloca, Donald G. Truhlar,* and Jiali Gao*

Department of Chemistry and Minnesota Supercomputing Institute, University of Minnesota, Minneapolis, Minnesota 55455

Received May 19, 2003; Revised Manuscript Received August 17, 2003

ABSTRACT: We have studied the hydride transfer reaction catalyzed by the enzyme dihydrofolate reductase (DHFR) and the coenzyme nicotinamide adenine dinucleotide phosphate (NADPH); the substrate is 5-protonated 7,8-dihydrofolate, and the product is tetrahydrofolate. The potential energy surface is modeled by a combined quantum mechanical-molecular mechanical (QM/MM) method employing Austin model 1 (AM1) and a simple valence bond potential for 69 QM atoms and employing the CHARMM22 and TIP3P molecular mechanics force fields for the other 21 399 atoms; the QM and MM regions are joined by two boundary atoms treated by the generalized hybrid orbital (GHO) method. All simulations are carried out using periodic boundary conditions at neutral pH and 298 K. In stage 1, a reaction coordinate is defined as the difference between the breaking and forming bond distances to the hydride ion, and a quasithermodynamic free energy profile is calculated along this reaction coordinate. This calculation includes quantization effects on bound vibrations but not on the reaction coordinate, and it is used to locate the variational transition state that defines a transition state ensemble. Then, the key interactions at the reactant, variational transition state, and product are analyzed in terms of both bond distances and electrostatic energies. The results of both analyses support the conclusion derived from previous mutational studies that the M20 loop of DHFR makes an important contribution to the electrostatic stabilization of the hydride transfer transition state. Third, transmission coefficients (including recrossing factors and multidimensional tunneling) are calculated and averaged over the transition state ensemble. These averaged transmission coefficients, combined with the quasithermodynamic free energy profile determined in stage 1, allow us to calculate rate constants, phenomenological free energies of activation, and primary and secondary kinetic isotope effects. A primary kinetic isotope effect (KIE) of 2.8 has been obtained, in good agreement with the experimentally determined value of 3.0 and with the value 3.2 calculated previously. The primary KIE is mainly a consequence of the quantization of bound vibrations. In contrast, the secondary KIE, with a value of 1.13, is almost entirely due to dynamical effects on the reaction coordinate, especially tunneling.

1. INTRODUCTION

Dihydrofolate reductase (DHFR) catalyzes the reduction of 7,8-dihydrofolate (DHF) to 5,6,7,8-tetrahydrofolate (THF) through the oxidation of the coenzyme nicotinamide adenine dinucleotide phosphate (NADPH). Figure 1 shows a schematic representation of the crystal structure of DHFR, and Figure 2 depicts the substrate and coenzyme. DHFR plays a key role in maintaining intracellular pools of tetrahydrofolate, which is a coenzyme in a number of one-carbon metabolic processes and is essential for the biosynthesis of purines, thymidylate, and several amino acids. The DHFR enzyme has long been recognized as a target for anticancer and antibacterial drugs (*1*). The importance of DHFR both in biological function and clinical application have led to numerous experimental and theoretical studies, including studies aimed at determining the catalytic mechanism of this enzyme.

† This work was supported in part by the National Science Foundation (D.G.T.) through Grant No. CHE00-92019 and by the National Institutes of Health (J.G.). M.G.-V. acknowledges financial support by the Fulbright Commission and a Government of Catalonia Scholarship Award.

In the simple Michaelis−Menten mechanistic scheme

$$E + S \underset{}{\overset{k_M}{\rightleftharpoons}} ES \xrightarrow{k_{cat}} E + P$$

the catalytic constant, k_{cat}, represents the maximum number of substrate molecules converted to products per active site per unit time. In general, the transformation of ES to E + P involves the formation of intermediates and multiple steps, including the release of the product. In the DHFR reaction, early kinetic investigations by Fierke et al. (*2*) and Morrison et al. (*3*) showed that product release is the rate-limiting step and that the enzyme-catalyzed chemical transformation is exceptionally efficient.

The overall reaction of DHFR involves addition of a proton and a hydride ion to DHF (Figure 2). At neutral pH, k_{cat} has a value of 450 s^{-1} at 298 K,[2] and at this pH the main contribution to limiting the rate comes from the release of tetrahydrofolate. The rate constant for hydride transfer from NADPH to DHF is pH-dependent and large at pH = 6.5, with a value of 950 s^{-1}; this step is essentially irreversible, due to its high K_{eq} of 1700 (*2*). The hydride transfer catalyzed by *Escherichia coli* DHFR (EcDHFR) becomes

10.1021/bi034824f CCC: $25.00
Published on Web 10/21/2003

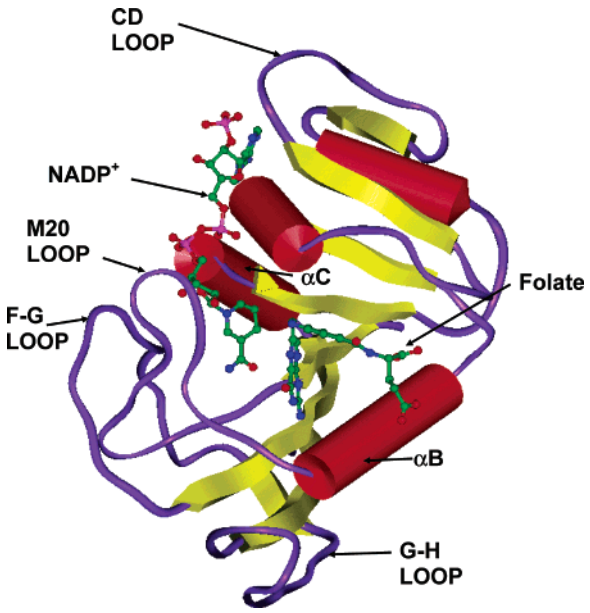

FIGURE 1: X-ray structure (PDB code 1RX2) of the ternary complex between *Escherichia coli* dihydrofolate reductase enzyme, folate substrate, and $NADP^+$ coenzyme. The heavy atoms of the ligands are represented in ball-and-stick model. The α helices are labeled αB and αC.

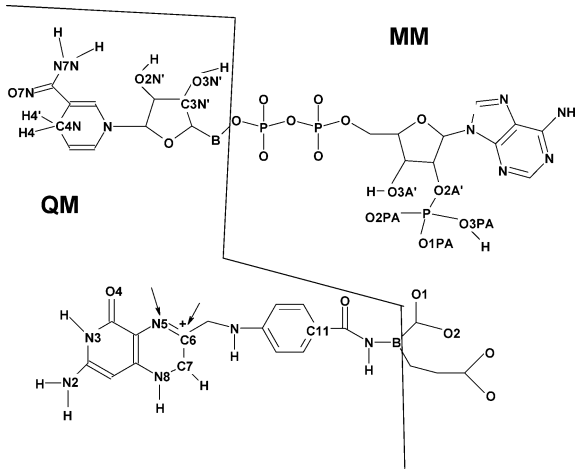

FIGURE 2: Schematic representation of the NADPH coenzyme (top) and 7,8-dihydrofolate substrate (bottom). Labels have been given to the atoms that are cited in the text. The two arrows indicate the positions where a proton (N5 position) and a hydride (C6 position) are added to give the final product, 5,6,7,8-tetrahydrofolate. The solid line divides the quantal and classical regions in the QM/MM simulations, and the two boundary atoms (which are both carbon) are marked with "B".

rate limiting at high pH, as shown by the dependence of the primary kinetic isotope effect (KIE) of k_{cat} on pH, and this strongly suggests that the protonated substrate is the reactive species for the hydride transfer reaction (*2*). However, X-ray structures show no direct interaction between the only ionizable residue (Asp 27) in the active center and the proton acceptor atom (N5 in Figure 2), and this makes it difficult to map the proton-transfer pathway (*4*, *5*). Although several experimental (*4*−*7*) and computational studies (*8*−*10*) have provided insight, the proton-transfer mechanism is not well-established yet.

Other aspects of the catalytic cycle of DHFR have also been intensively investigated. For example, it has been shown experimentally that the catalytic cycle involves conformational changes (*11*−*18*). On the basis of X-ray crystallographic data on EcDHFR, Sawaya and Kraut (*14*) proposed that the conformational changes of the M20 loop (the active site loop of DHFR, see Figure 1) modulate the ligand specificity observed in the catalytic cycle. A possible reason for the flexibility of the M20 loop in EcDHFR is to increase the affinity for NADPH versus $NADP^+$ (*14*, *19*), which is not necessary in human DHFR because in eukaryotic cells the concentrations of $NADP^+$ are no more than 1% of NADPH concentrations. Thus, EcDHFR and human DHFR have different catalytic pathways and binding affinities for substrates and products. Because of the evolutionary divergence of EcDHFR from mamalian DHFR and even from other bacterial DHFRs (*19*), we will concentrate further discussion only on EcDHFR. Mutation studies (*13*, *15*, *16*) of EcDHFR have shown that deletion of residues on the M20 loop and the neighboring F−G loop (Figure 1) has a large impact on the rate constant of the hydride transfer step. These mutation effects together with the results obtained in NMR studies (*11*, *12*, *17*) support a mechanistic model in which interloop contacts regulate an equilibrium of M20 loop conformations, and, in turn, this equilibrium modulates ligand affinity and turnover (*16*, *18*, *20*).

In several mutagenesis experiments, Benkovic and coworkers found nonadditive effects for distant double mutants (*21*, *22*). A recent molecular dynamics simulation showed that the interactions of the mutated residues are correlated (*23*). Importantly, these correlated interactions occur in many of the same regions of the protein identified as highly flexible regions in the dynamic NMR measurements (*12*, *17*, *20*). It was also suggested that motions of key residues in the active site play an important role in catalysis by promoting the hydride transfer step (*24*−*26*). However, Agarwal et al. pointed out (*24*) that it is difficult to distinguish whether the effect of the mutations is to uncouple the motions between the residues or to cause conformational changes that alter the reactive orientation of the substrate with respect to the coenzyme; this orientation is found to be governed by interactions with distant residues. The molecular dynamics simulations have been extended (*27*) to studying the effect of the mutation of Gly-121 to valine, which reduces the rate of the hydride transfer by a factor of 163 (*13*); the simulation indicates that the reduction is due to an increase in the free energy barrier. These calculations show that some of the changes in interaction distances that are observed in the active site of the wild-type enzyme in going from the Michaelis complex to the transition state are not found in the mutant enzyme (*27*). These studies (*20*−*27*) have identified dynamical motions of various residues in DHFR that are proposed to be coupled to the catalytic transformation.

Recently, Thorpe and Brooks (*28*) calculated the energy profiles along the reaction coordinate for the hydride transfer in the wild-type enzyme and the G121S and G121V mutants by a combined quantum-mechanical and molecular-mechanical (QM/MM) method. They analyzed the correlation between the hydride transfer barrier calculated for different enzyme configurations and the change of a selected set of geometric parameters. The geometrical changes in the wild-type enzyme are found to agree with the results obtained by Agarwal et al. (*25*), although most of the enzyme atoms are fixed in the calculations. This led Thorpe and Brooks to

suggest that coupled promoting motions are not essential and that the difference in reaction rates between the wild-type and mutant enzymes may be explained by quasithermodynamic contributions (*28*).

The effects of the enzyme electric field on the molecular polarization of the NADPH coenzyme and the substrate were investigated by Bajorath et al. (*29*) and Greatbanks et al. (*30*). These authors used calculations on a single structure to analyze the differences between the atomic partial charges of the ligands in the enzyme environment and in the gas phase. Those studies have been extended by calculating the energetic consequences of charge polarization of ensembles of reactant, transition state, and product complexes along the reaction path of the hydride transfer step (*31*).

Additional computational studies have focused on the kinetics of the hydride transfer step. The free energy profile for the hydride transfer from NADPH to the 8-methylpterin substrate has been computed using a QM/MM potential (*32*). The primary KIE has been estimated using a QM/MM potential and transition state theory (TST) based on electronic-energy structure optimization (*33*). Using molecular dynamics coupled with a multiconfiguration self-consistent field method that included nuclear quantum mechanical effects on the transferred atom, Agarwal et al. (*25*) also computed a free energy profile for the hydride transfer step.

The present paper describes a new study of the kinetics of the hydride transfer reaction from NADPH coenzyme to 5-protonated 7,8-dihydrofolate substrate. We use a combined QM/MM (*34*−*36*) potential energy surface and ensemble-averaged variational transition state theory with multidimensional tunneling contributions (EA-VTST/MT) (*37*, *38*) to calculate primary and secondary KIEs, which provide unique information about catalytic mechanisms (*39*). As mentioned above, the hydride transfer reaction catalyzed by *E. coli* DHFR becomes rate limiting at high pH (*2*), as shown by the measured KIE. In the present study, however, we validate the computational method by comparing the calculated k_{cat} and primary KIE for the hydride transfer step at neutral pH to experimental results for the hydride transfer step determined at a similar pH (*2*), namely, pH 6.5. We also predict the secondary KIE.

2. THEORY

In the present work, we have modeled the potential energy surface (PES) by a combined QM/MM approach (*34*−*36*) that includes the generalized hybrid orbital (GHO) (*36*) method to treat the boundary between the QM and the MM fragments of the system. In addition, we use a simple valence bond (SVB) (*40*) term to improve the accuracy of the PES.

The rate constants and KIEs have been determined by the ensemble-averaged variational transition state theory with the multidimensional tunneling EA-VTST/MT method, the formalism of which has been presented in detail in recent papers (*37*, *38*, *41*). In brief, the rate constant for the hydride transfer step in DHFR is written as follows:

$$k(T) = \gamma(T)k^{(1)}(T) = \gamma(T)\frac{1}{\beta h}\exp[-\beta\Delta G^{(1)}_{act}(T)] \quad (1)$$

where h is Planck's constant, $\beta = 1/\tilde{k}T$, $\tilde{k}$ is Boltzmann's constant, $\gamma(T)$ is the overall transmission coefficient, $k^{(1)}$ is the quasithermodynamic rate constant, and $\Delta G^{(1)}_{act}$ is the quasithermodynamic free energy of activation, which includes the quantum mechanical (QM) vibrational free energy. Both $k^{(1)}$ and $\Delta G^{(1)}_{act}$ correspond to a distinguished reaction coordinate z, and they are labeled with the superscript (1) because the steps of the calculation employing this distinguished reaction coordinate are called stage 1. (In stage 2, which is the calculation of the transmission coefficient, we introduce an ensemble of more accurate reaction coordinates, called s (*37*, *38*, *41*), and this allows the entire system to participate in the effective reaction coordinate at that stage.) In summary, the two quantities needed to estimate the rate constant are the quasithermodynamic free energy of activation and the transmission coefficient.

The quasithermodynamic free energy of activation is obtained by first calculating the classical mechanical potential of mean force (PMF), $W^{CM}(z)$, as a function of the distinguished reaction coordinate. This PMF, $W^{CM}(z)$, is called classical mechanical (CM) because it is computed in Newtonian molecular dynamics simulations without quantizing nuclear motions, and the CM free energy of activation is obtained by (*37*)

$$\Delta G^{CM}_{act} = W^{CM}(z^{CM}_*) - W^{CM}(z_R) - G^{CM}_{R,F} \quad (2)$$

where z^{CM}_* is the value of the reaction coordinate corresponding to the maximum of $W^{CM}(z)$, z_R is the value of z at the reactant (R) minimum of $W^{CM}(z)$, and $G^{CM}_{R,F}$ is the free energy of the normal mode (F) that corresponds to z at z_R. In general, we choose the zero of energy of $W^{CM}(z)$ so that $W^{CM}(z_R) = 0$.

The quantization of the classical free energy is achieved by adding a quantum mechanical vibrational correction, $\Delta W_{vib}(T,z)$, to $W^{CM}(z)$ (*37*, *42*). We employed two methods for including quantized vibrations in the classical free energy of activation. Both methods start by calculating the frequencies $\omega_{m,j}$ of the generalized normal modes (*42*, *43*) m for a subset of atoms in the active site, called the primary zone of the system, at an instantaneous configuration j (see section 3.3.2 for more details of this part of the calculation). The first method, called the average frequency (AF) method, is the one used previously (*37*, *41*, *42*). In this method, we first calculate average frequencies

$$\bar{\omega}_m(z_b) = \langle\delta(z - z_b)\omega_{m,j}\rangle \cong \frac{1}{J_b}\sum_{j=1}^{J_b}\omega_{m,j} \quad (3)$$

where z_b is the value of z at the center of a bin of width 0.01 Å, J_b is the number of configurations at which frequencies are calculated in bin b, and $J = \sum_b J_b$ is the number of configurations used to make the quantum correction. (Note that J is being defined for later use in section 3.3.2.) Then, the difference between the quantized and classical mechanical free energies is estimated by

$$\Delta W^{AF}_{vib}(z_b) = W^{Q}_{vib}(\{\bar{\omega}_m(z_b)\}) - W^{C}_{vib}(\{\bar{\omega}_m(z_b)\}) \quad (4)$$

where W^{Q}_{vib} and W^{C}_{vib} are, respectively, the quantized and classical mechanical expressions (*42*) for the vibrational free energy of a collection of harmonic oscillators, and $\{\bar{\omega}_m(z_b)\}$ denotes the set of frequencies $\bar{\omega}_m(z_b)$ in the collection. In the second method, called the perturbation (P) method, we replace eq 4 by

$$\exp[-\Delta W^{P}_{vib}(z_b)/\tilde{k}T] = \langle \delta(z - z_b) \times \exp[-[W^{Q}_{vib}(\{\omega_{m,j}\}) - W^{C}_{vib}(\{\omega_{m,j}\})]/\tilde{k}T]\rangle = \frac{1}{J_b}\sum_{j=1}^{J_b}\exp[-[W^{Q}_{vib}(\{\omega_{m,j}\}) - W^{C}_{vib}(\{\omega_{m,j}\})]/\tilde{k}T] \quad (5)$$

The correction function $\Delta W_{vib}(T,z_b)$ evaluated at the sequence of z_b values is fitted to a continuous function $\Delta W_{vib}(T,z)$. Adding $\Delta W_{vib}(T,z)$, calculated with either method, to $W^{CM}(z)$ gives the quasithermodynamic potential of mean force, $W^{(1)}(z)$ (*37*), that contains quantized vibrations for the primary zone, except one degree of freedom corresponding to the reaction coordinate, z:

$$W^{(1)}(T,z) = W^{CM}(T,z) + \Delta W_{vib}(T,z) \quad (6)$$

The quasithermodynamic transition state free energy of activation, $\Delta G^{(1)}_{act}$ in eq 1, is obtained by

$$\Delta G^{(1)}_{act} = W^{(1)}(z^{QC}_{*}) - W^{(1)}(z_R) - G^{QC}_{R,F} \quad (7)$$

where $z^{(1)}_{*}$ is the coordinate at the maximum of $W^{(1)}(z)$, and $G^{QC}_{R,F}$ is the quantized value of $G^{CM}_{R,F}$ (*37*).

In the present study, the transmission coefficient is computed in the static secondary zone approximation (*37*) from a transition state ensemble optimized on the basis of free energy; the use of such an ensemble provides a more realistic and complete treatment than using only a single structure optimized on the basis of electronic energy. The transmission coefficient is the product of two factors, Γ and κ. The first factor, which is the quasiclassical transmission factor, Γ, corrects the rate constant for dynamical recrossing (*37*, *44*); this factor is calculated quasiclassically, which, in this context, refers to the fact that some degrees of freedom are quantized, but the reaction coordinate is not. The second factor, κ, is the semiclassical transmission coefficient that accounts mainly for tunneling, that is, the quantum mechanical effects on the motion along the reaction coordinate, which are missing in the quasithermodynamic calculation of the $k^{(1)}$ rate constant. (In the present context, "semiclassical" refers to the use of a multidimensional WKB-like approximation to compute the quantum effects.) The primary such effect is quantum mechanical tunneling, but the κ factor also includes nonclassical reflection (*43*) by the barrier (this latter effect is a diffraction effect by which a small fraction of the particles that have enough energy to surmount the barrier are nevertheless reflected by it). The calculations carried out to determine the Γ and κ factors involve an ensemble average (*37*, *38*) over an equilibrium distribution of secondary-zone configurations, labeled $i = 1, 2, ..., I$, corresponding to $z = z^{(1)}_{*} \pm \Delta z$, where $z^{(1)}_{*}$ is the location of the stage 1 variational transition state (also called the quasithermodynamic transition state), which is located at $z = z^{(1)}_{*}$, and Δz is 0.005 Å. For each transition state configuration i, we freeze the secondary-zone atoms to calculate an isoinertial minimum energy path (MEP). The individual paths obtained for the different configurations i describe the dynamics of the primary-zone atoms under the effective potential of the rest of the system for the various configurations. For each configuration, we first calculate the Γ_i factor, which is a function of the difference in free energy between its maximum in the MEP calculation and its value at the point for which z equals to $z^{(1)}_{*}$ (*37*, *41*). The introduction of the classical recrossing correction, given by the average value of Γ, $\Gamma(T) = \langle\Gamma_i\rangle$, to the transition state rate constant $k^{(1)}$ gives the final quasiclassical rate constant:

$$k^{QC}(T) = \Gamma(T)k^{(1)}(T) \quad (8)$$

Then individual semiclassical transmission coefficients κ_i are calculated by employing methods fully described in previous work (*43*, *45*, *46*). The product of the two factors, κ_i and Γ_i, gives the net transmission coefficient for configuration i.

$$\gamma_i = \kappa_i\Gamma_i \quad (9)$$

Averaging the total transmission coefficient γ_i over i secondary-zone configurations gives the final static-secondary-zone rate constant of eq 1, where $\gamma(T) = \langle\gamma_i\rangle$.

The final theoretical estimate of the phenomenological free energy of activation is

$$\Delta G_{act} = \Delta G^{(1)}_{act} - RT\ln\gamma \quad (10)$$

More details about the dynamics methods used in this work are given in section 3.3.2.

3. COMPUTATIONAL DETAILS

3.1. Model of the Enzyme−Substrate−Coenzyme Complex in Water. Sawaya and Kraut (*14*) have resolved a set of isomorphous crystal structures that are proposed to be analogous to the five detectable kinetic intermediates in the catalytic cycle of *E. coli* DHFR. On the basis of these structures, it has been inferred that the M20 loop (Figure 1) is predominantly closed over the reactants in the holoenzyme, Michaelis complex, and transition state. The structure (PDB code 1RX2) used to build the model for the present study corresponds to the Michaelis complex with the M20 loop (residues 10−24) in the closed conformation. The crystal structure contains a total of 159 amino acid residues, 153 crystallographic waters, and the folate and $NADP^+$ ligands, which were replaced by 7,8-dihydrofolate and NADPH, respectively, for the simulation. Key interactions (*14*) responsible for coenzyme binding include hydrogen bonds involving Ile14, Gly15, Glu17, Asn18, and Asp122 (Figure 3). The F−G loop (residues 116−125) and the helix C (residues 44−50) interact with the M20 loop, positioning it to interact with the coenzyme (*14*). These interactions are characteristic of the closed conformation (*14*), and therefore we have monitored them along the simulated reaction, as a validation for the model used.

The coordinates for hydrogen atoms of the protein and the coenzyme were determined using the HBUILD facility in the program CHARMM (*47*). On the basis of the results of Callender and co-workers (*5*, *7*), we assumed that Asp27 is deprotonated at neutral pH, as it would be in bulk water. The protonation states for all other ionizable residues were set corresponding to pH 7 (which is reasonable since the experiment we compare to corresponds to pH 6.5). Thus, histidine residues were modeled as neutral residues with the proton on Nϵ or Nδ as determined on the basis of possible hydrogen bond interactions deduced from the X-ray crystal-

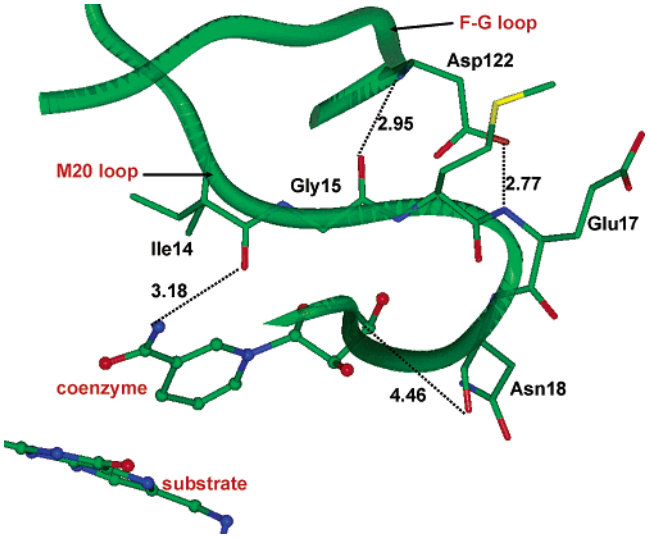

FIGURE 3: Partial view of the active center of DHFR (PDB code 1RX2). The position of the M20 and F−G loops, the nicotinamide and ribose rings of the coenzyme, and the pterin ring of the substrate are shown. The numbers indicate the distances found in the X-ray structure for interactions that are proposed to characterize the M20 loop closed conformation.

lographic structure. The substrate molecule was protonated at the N5 position to model the protonated 7,8-dihydrofolate (Figure 2). The resulting system has a net charge of −15 e, which was neutralized by placing sodium cations near negatively charged residues at distances greater than 17 Å from the active center. The final protein structure was solvated with a previously equilibrated cubic box of water molecules, centered at the geometric center of the protein ternary complex. The initial dimensions of the box were 60 × 60 × 60 Å^3, which ensures that all protein atoms are at least 8 Å away from the edges of the box. Water molecules that are within 2.5 Å of any non-hydrogen atoms of the protein or ligand were removed. The final model contains 21 468 atoms, of which 2489 are protein atoms.

For comparison, an analogous model was built to study the hydride transfer reaction from NADPH to the nonprotonated 7,8-dihydrofolate substrate.

3.2 Potential Energy Surface. To equilibrate the solvated protein system, we first carried out molecular dynamics simulations using the all-atom CHARMM22 (*48*) force field to represent the protein, substrate, and coenzyme (*48b*) and using the three-point-charge TIP3P (*49*) model for water. The parameters for the 5-protonated 7,8-dihydrofolate substrate were derived from standard parameters for analogous functional groups along with results from ab initio calculations. Mulliken population charges (*50*) that were determined using the QM/MM model described below were assigned to the QM atoms of the 5-protonated DHF substrate and to the nicotinamide and ribose atoms of the coenzyme. A list of all new parameters determined this way is given in the appendix. We note that these parameters were used only for the purpose of initial equilibration of the system. They are not designed for quantitative calculations, nor were they used to determine the properties reported in this paper (because in the final calculations we did not use molecular mechanics for these atoms).

For combined QM/MM calculations, the system was partitioned into a quantum mechanical region consisting of

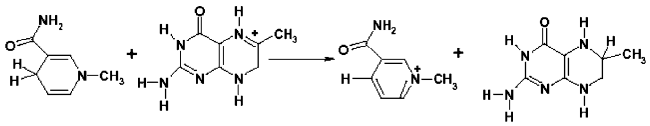

FIGURE 4: Model reaction for the hydride transfer step.

Table 1: Energy of Reaction[a] for the Model Reaction of Figure 4

method	Δ*E* (kcal/mol)
AM1	14.0
PM3	15.4
HF/6-31G(d,p)	−6.6
B3LYP/6-31G(d)	−6.2
mPW1PW91/6-31+G(d)	−7.1

[a] Excluding zero-point contributions in all cases.

69 atoms and a molecular mechanical region containing the rest of the system. The QM system includes 39 atoms from the 5-protonated 7,8-DHF substrate (the pteridine ring, the *N*-methylene-substituted *p*-aminobenzoic acid (pABA) moiety, and the −NH−C_α group of the glutamate moiety) and 30 atoms from the NADPH coenzyme (the dihydronicotinamide and ribose rings). This is illustrated in Figure 2. The QM subsystem contains two boundary atoms: the C_α at the glutamate residue and the C5′ ribose atom, which are represented by the GHO method (*36*).

We used the semiempirical Austin model 1 (*51*) (AM1) to describe the QM subsystem. To validate the performance of the AM1 model and to make corrections to improve its accuracy, we carried out gas-phase ab initio molecular orbital and hybrid density functional calculations for the model reaction represented in Figure 4. Geometry optimizations and energies were computed at the AM1, PM3 (*52*), HF/6-31G(d,p), B3LYP/6-31G(d), mPW1PW91/6-31+G(d) levels of theory. The latter hybrid density functional theory (HDFT) has been shown to be especially accurate (*53*, *54*), and it will be used as a standard for testing the semiempirical methods. The results for the energy of reaction of the model reaction are compared in Table 1. The AM1 semiempirical level was chosen in the present study because of its overall performance. However, the deviation from HDFT results was too large to be ignored for quantitative work. Consequently, we introduced a simple valence bond (SVB) term (*40*) to correct the energies at the critical points on the potential energy surface. This correction includes two Morse terms, which correct the error in the difference of the heterolytic bond dissociation energies for the two-half hydride transfer reactions. The form of the SVB potential is given as follows:

$$V_{SVB} = \frac{1}{2}[M_1(r_{DH}) + M_2(r_{AH}) - \sqrt{((M_2(r_{AH}) - M_1(r_{DH}))^2 + 4V_{12}^2}] + D_1 \quad (11)$$

where $M_i(r_i)$ is a Morse potential given by

$$M_i(r_i) = D_i[e^{-2\alpha_i(r_i - r_i^o)} - 2e^{-\alpha_i(r_i - r_i^o)}] \quad (12)$$

and V_{12} is a coupling element. Although one might take V_{12} to be a function of the donor−acceptor distance or other geometrical variables in the general case, in the present work it was taken as a constant for simplicity. Therefore, there are seven parameters. In eq 11, the donor species (DH)

Table 2: Parameters for the Simple Valence Bond (SVB) Potential for the Hydride Transfer Reaction in Dihydrofolate Reductase

	D_i (kcal/mol)	α_i (Å^{-1})	r_i^0 (Å)	V_{12} (kcal/mol)
C4N−H	245.7	0.4	1.10	
C6−H	214.1	0.5	1.11	
C4N−C6				23.0

denotes the nicotinamide ring and the acceptor (AH) specifies the pterin ring.

The final QM(AM1-SVB)/MM potential energy surface (PES) is

$$V = V_{QM/MM} + V_{SVB} \quad (13)$$

where the first term is the QM/MM potential based on AM1 (*51*), the CHARMM22 protein force field (*48*), and the TIP3P model for water (*49*).

We parametrized the SVB term in this PES to reproduce (after adding an estimation of the quantum and dynamical corrections to the classical free energy of reaction and to the TST rate constant, respectively) the experimental free energy of reaction of −4.4 kcal/mol, which is calculated from the reported (*2*) value (1700) of K_{eq}, and the experimental free energy of activation of 13.4 kcal/mol, calculated from the phenomenological rate constant (*2*) for the hydride transfer step using transition state theory. To accomplish this, we repeated the calculations of the potential of mean force on the QM(AM1-SVB)/MM PES with different trial sets of SVB parameters. The final parameters are listed in Table 2.

3.3. Simulations. 3.3.1. The Michaelis Complex Preparation. To remove close contacts and highly repulsive orientations of the initial protein−solvent system, we first performed 100 steps of energy minimization for all water molecules using the adopted-basis set Newton−Raphson (ABNR) method in CHARMM-version c28 (*47*), with the protein atoms held fixed. This was followed by 100 steps of restrained energy minimization of the entire system; the restraints were harmonic potentials applied to atoms in the coenzyme and substrate and to the protein backbone atoms. From the resulting configuration, molecular dynamics (MD) simulations with periodic boundary conditions (PBC) and the isothermal−isobaric (NPT) ensemble at 298 K and 1 atm were carried out to obtain the average volume of the system. The constant pressure and temperature calculations were carried out using the CRYSTAL module of CHARMM-version c28; in this method, a crystal is constructed by surrounding the cubic primary cell (the ternary complex, the cubic box of waters, and the counterions) with 26 identical images. In practice, only the images within a given cutoff are generated when a cutoff criterion is used to reduce the number of nonbonded interactions, and in all the calculations of the present study, a spherical cutoff distance of 12 Å was used for the nonbonded interactions along with a switch function in the region 11−12 Å to feather the interaction energy to zero. The nonbonded pair list and the image list were built on the basis of group separations, and they were updated every 30 and 120 steps, respectively. During an image update, the distant solvent molecules were replaced by a close image, and the group of image atoms within the cutoff distance of the primary atoms was updated.

We used the leapfrog integration scheme (*55*) to propagate the equations of motion with a time step of 1 fs and with the extended system constant pressure and temperature algorithm implemented in CHARMM (*56*−*58*). All bond lengths and bond angles involving hydrogen atoms were constrained by the SHAKE algorithm (*59*), and the dielectric constant was set to 1.

Initially, the temperature of the system was gradually raised from 0 to 298 K in 30 ps of molecular dynamics, with the system under harmonic restraints using the crystallographic structure as the reference. Then, the harmonic restraints on the protein atoms were gradually released during a further 50 ps simulation at 298 K. At this stage, the harmonic force constants used for the restraints on the heavy atoms of the pteridine ring of the substrate and the nicotinamide ring of the coenzyme were decreased to a value of 1 kcal mol^{-1} Å^{-2}, but not completely eliminated. This ensured that the relative orientation of the hydride-donor and hydride-acceptor rings, found in the X-ray structure, was maintained. This was necessary because nonstandard MM parameters listed in the appendix were used for the substrate atoms in this stage. At this point, we considered that the system was equilibrated because of the small value of the fluctuation in temperature (2 K) and total energy (0.3% of the average value) over the last 10 ps. The average length of the box edge in the last 10 000 steps (10 ps) of the 50 ps run was 58.93044 Å, which was used in the subsequent QM/MM molecular dynamics simulations at constant volume and temperature. This average length is 2% smaller than the average length of the original box edge.

The QM/MM simulations were carried out using periodic boundary conditions and the same nonbonded cutoff, switching functions, and dielectric constant as in the MM calculations, but we used an algorithm that takes advantage of the minimum image convention for a periodic cubic box. The procedure is an extension of that implemented into CHARMM by Shirley and Brooks (*60*) for MM calculations, which avoids the generation (that is required in the standard CRYSTAL module) of image atoms in addition to atoms in the primary cell. The solvent molecules (water and counterions) were translated every 1000 steps to their image position closest to the center of the system, which is defined as the geometric center of the protein−ligands complex. The center of the protein−ligands complex was updated at each nonbonded pair list update. All the hydrogen atoms, with the exception of the hydrogens attached to the C4N atom of the NADPH coenzyme, were constrained by the SHAKE (*59*) algorithm. The velocity Verlet algorithm (*61*) and the Nosé-Hoover (*56*, *57*) constant temperature algorithm were used to run these simulations at 298 K and at constant volume on the QM(AM1-SVB)/MM potential energy surface described above. After 10 ps of restrained MD simulations, using the restraints applied during the last 20 ps of the classical MM simulation, the system was allowed to move completely freely for 50 ps. Overall, the equilibration phase included 140 ps of MD simulations, of which 80 ps were based on MM potentials and 60 ps were based on QM/MM potentials, to prepare the starting configuration of the Michaelis complex for free energy simulations.

3.3.2. Dynamics. The potential of mean force (PMF) $W^{CM}(z)$ was determined using the umbrella sampling technique (*62*−*64*) along the reaction coordinate z, which is defined geometrically (*38*, *65*) as the difference between the C4N−H4 distance r_{form} and the H4−C6 distance r_{break}.

In the present study (Figure 4):

$$z = r_{break} - r_{form} \quad (14)$$

A total of 18 separate simulations (or windows) were executed to span the entire range of the reaction coordinate from reactants to products. Each simulation was performed with the addition of a biasing potential, roughly the negative of the final computed PMF, and a harmonic restraining potential centered at the location (z_i^0) of that particular window. For each window of these calculations, the velocities and positions of the last configuration generated in the previous window were used to initiate the next window, which was equilibrated for 15 ps, and the probability density of configurations along z was collected for an additional 40 ps and sorted into bins of width 0.01 Å. The uncertainty in the reaction coordinate is half of the bin size, 0.005 Å. To estimate the simulation error and to increase the efficiency of sampling, we carried out two series of these calculations, one starting from the reactant side and one from the product side.

Each of these two series of simulations has a total length of 990 ps. During the umbrella sampling simulations, the trajectory was saved at intervals of 100 steps for the simulation started from the reactant side and intervals of 10 steps from the product state.

The $W^{CM}(z)$ curve was first obtained from these separate series of simulations by manually matching, at the point of maximum overlap in probability density of configurations, the free energy profiles obtained from consecutive windows. We then repeated the analysis of the data obtained by the two separate series of simulations with the weighted histogram analysis method (WHAM) (*62*, *64*). The results obtained by manually matching the free energies of consecutive windows and the ones obtained by the WHAM method differ by less than 0.82 kcal/mol at all values of z between the reactant and the product states. A final $W^{CM}(z)$ was obtained by combining the probability density of configurations obtained from both series of simulations in the WHAM analysis (*62*−*64*).

For subsequent calculations, we used structural information from the simulation started at the reactant state to estimate KIEs by employing the CHARMMRATE (*66*) module of CHARMM (*47*), based on interface of CHARMM and POLYRATE (*67*). We investigated three different systems and determined the primary and secondary KIEs: (i) the nicotinamide ring with protium atoms at H4 and H4′ positions (labeled HH substitution, Figure 2), (ii) the replacement of protium by a deuterium atom at position H4 (labeled DH substitution), and (iii) the deuterium replacement at position H4′ (labeled HD substitution). Note that position 4 labels the atom transferred, and 4′ labels the spectator.

The quantized-vibration correction (*42*) to the computed potential of mean force was obtained from instantaneous generalized normal-mode frequencies (*37*, *42*) of the primary-zone atoms for 694 configurations generated along the umbrella sampling simulation path ($J = 198$ configurations from two windows at the reactant state, $J = 198$ configurations from two windows at the product state, and $J = 298$ configurations from the transition state region). The same configurations were used to calculate the quantized-vibration correction to the PMF for the isotopically substituted cases.

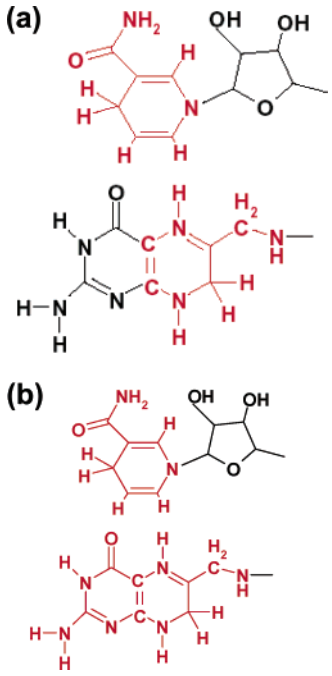

FIGURE 5: (a) Schematic representation of the primary zone atoms (in red) used for the calculation of the quantum mechanical vibrational free energy correction. (b) Schematic representation of the primary zone atoms (in red) used for the dynamics calculations.

For each configuration, the instantaneous generalized normal-mode frequencies were determined for the 31 atoms of the primary zone defined in Figure 5a. The Hessian was determined numerically by a central difference scheme with a step size of 0.0053 Å, and the generalized normal modes were calculated in rectilinear coordinates (*43*). When calculating generalized normal-mode frequencies, the reaction coordinate was projected out of the Hessian, as described in refs *37* and *42*. The calculated frequencies for the various configurations were averaged over all the configurations that belong to a given bin of width 0.01 Å, and the correction of eq 4 was calculated as a function of the averaged frequencies. For the HH case, we also calculated eq 5.

We chose the configurations for the transition state ensemble (TSE) from the classical simulation, and these configurations were used to calculate the averaged transmission coefficient of eq 9. In previous work (*37*, *41*, *65*, *68*), this selection was made by using samples that were approximately evenly spaced in time; however, in the present work, we used a better prescription; in particular, we chose the members of the TSE on the basis of their closeness to $z_*^{(1)}$. In each window of the umbrella sampling simulation, 400 configurations were saved, and the TSE consisted of the saved configurations with z values closest to $z_*^{(1)}$ (within 0.01 Å). In calculating the transmission coefficient, the primary zone is somewhat larger than the one used above to make quantum corrections to the PMF. In particular, we included all the atoms of the pteridine ring (Figure 5b), so that the total number of dynamical atoms is 40. Geometry optimizations of the primary zone reactant and product species were performed using the BFGS method (*69*), while the saddle point geometry was obtained using the Newton−Raphson method with Brent line minimization (*70*) with the gradient converged to 1.2×10^{-4} kcal mol^{-1} Å^{-1}. The reaction path was traced using the Euler steepest descent

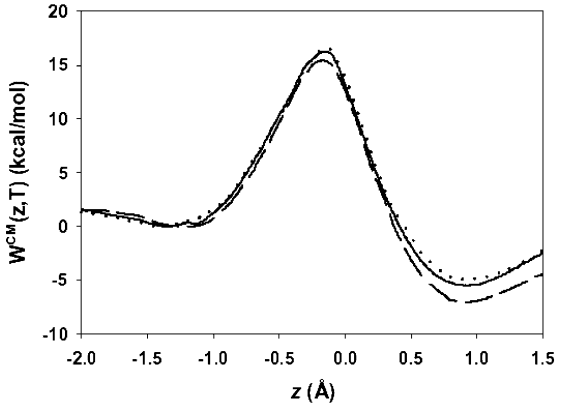

FIGURE 6: Classical mechanical potentials of mean force (CM PMF). The dotted curve is from manually matching the series of simulations started at the reactant side, the dashed curve is from manually matching the series started at the product side, and the solid curve is obtained by WHAM (*62*−*64*) analysis using all the samples from both series of simulations.

method (*71*) in mass-scaled coordinates with a reduced mass of 1 amu and a step size of 0.00106 Å. The number of transition state configurations used to calculate transmission coefficients is $I = 13$.

The MT transmission coefficient, $\kappa_i(T)$, was microcanonically optimized between the small-curvature tunneling (SCT) value calculated by using the centrifugal-dominant small-curvature semiclassical adiabatic algorithm (*45*), and the large-curvature tunneling (LCT) value determined with the version 4 algorithm (*46b*).

4. RESULTS AND DISCUSSION

4.1. Potential of Mean Force and Free Energy of Activation. Figure 6 shows the potentials of mean force obtained from the two independent series of simulations started from the reactant and the product states, respectively. These two curves have been obtained by manually matching the free energy profiles calculated from consecutive windows. In addition, Figure 6 shows the combined PMF obtained from both simulations using the WHAM method (*62*−*64*). The largest deviation between the PMFs from the forward and backward simulations is about 2.1 kcal/mol. (Recall from section 2 that each PMF was zeroed on the reactant side.) The deviation of the two series of simulations is about 1 kcal/mol at the transition state. In a recent study, Thorpe et al. (*28*) found a broad range of values in the computed energy barrier height for the DHFR reaction. They obtained an effective energy of activation by averaging the barrier height of many potential energy profiles, which were determined by constrained energy minimization using a combined QM/MM potential for configurations that were saved in a 10 ns MD simulation (with time step of 2 fs). These authors argued that PMF-based approaches tend to sample a very localized set of configurations, and they are not able to capture the range of protein and solvent configurations that lead to such broad distributions (*28*). However, similar findings have been observed using configurations that were saved during umbrella sampling calculations (*37*, *41*, *68*), and Figure 6 also indicates that the computed PMF shows good convergence when tested by comparing simulations started at very different conformational substates of the enzyme (separated by 990 ps of MD simulation). Thus, it appears possible to get meaningful results from theoretically justified free energy sampling methods, and it is not necessary to use unconventional averaging methods.

The computed classical quasithermodynamic free energy of activation is 16.1 kcal/mol, which includes the correction due to the $G^{CM}_{R,F}$ term in eq 2. It turns out that $G^{CM}_{R,F}$ is 0.5 kcal/mol for all isotopic substitutions, namely, HH, DH, and HD, as obtained (from five configurations that were saved at the minimum on the reactant side at $z_R = -1.425$ Å) by a procedure that has been presented previously (*37*).

Figure 6 shows that the transition state of the CM PMF is located at $z^{CM}_* = -0.145$ Å. The average distance between the donor and the acceptor atom at z^{CM}_* is 2.68 Å, and the average C4N−H4−C6 angle is 157 deg. These values agree well with results obtained previously (*25*, *33*, *72*, *73*) for model reactions in the gas phase and for reaction in the enzyme.

4.2. Mechanism. The DHFR reaction formally involves the addition of H_2 to DHF, and, a priori, the proton-transfer step can proceed either before or after the hydride transfer reaction. The free energy reaction profile for the hydride transfer step in Figure 6 was obtained for the substrate after the protonation reaction at the N5 position of DHF. We have also calculated the potential of mean force for the hydride transfer reaction from NADPH to 7,8-dihydrofolate, i.e., the nonprotonated substrate, which yielded a free energy barrier of 48 kcal/mol, which is more than 30 kcal/mol greater than for the protonated substrate. In a recent study, Shrimpton et al. (*10*) concluded that the hydride transfer step might occur before the proton transfer because the average time during which water was found within hydrogen bonding distance of N5 was significantly increased when the hydride was transferred from NADPH to C6 of 7,8-dihydrofolate before protonation. However, this observation does not provide direct evidence for the sequence of reaction. On the other hand, the results from the free energy simulations in the present study demonstrate that the barrier for hydride transfer would be unrealistically high if the protonation step took place after the hydride transfer reaction. Furthermore, we found that a water molecule bridging the N5 and O4 atoms of the substrate 7,8-dihydrofolate is conserved throughout the simulation. Thus, we conclude that the reduction of DHF proceeds via an initial proton transfer, perhaps through a bridging water molecule, followed by hydride transfer, consistent with experimental (*3*) and computational (*8*, *9*) results.

4.3. Rate Constants and Degree of Tunneling. To evaluate rate constants for enzymatic reactions in the EA-VTST/MT method, two kinds of corrections are made to the rate constants determined using the free energy barrier from classical molecular dynamics simulations (Figure 6). The first is to include quantum mechanical effects, specifically zero-point energy, tunneling, and nonclassical reflection, and the second is to include dynamical recrossing in the transmission coefficient. We calculated the effect of quantizing vibrations, except one degree of freedom corresponding to the reaction coordinate, using both the average frequency (AF) and the perturbation (P) method (see section 2). The numerical results from the two computational methods agree within 0.05 kcal/mol for the HH case. Thus, the computed $\Delta W_{vib}(z)$ is not sensitive to whether this averaging step is carried out using

Table 3: Computed Rate Constants and Free Energies of Activation at 298 K for Three Isotopic Combinations

Rate Constants (s^{-1})

	$k^{(1)}(T)^a$	$k^{QC}(T)^b$	$k^{EA-VTST/MT}(T)^c$	$k_{hyd}(T)^d$
HH	638	477	1619	950
DH	232	191	572	317
HD	638	464	1433	

Free Energies of Activation (kcal/mol)

	$\Delta G_{act}^{(1)}$	ΔG_{act}^{QC}	$\Delta G_{act}^{EA-VTST/MT}$	ΔG_{act}
HH	13.6	13.8	13.1	13.4
DH	14.2	14.3	13.7	14.0
HD	13.6	13.8	13.1	

Kinetic Isotope Effects

HH/DH	2.75	2.50	2.83	3.00
HH/HD	1.00	1.03	1.13	

[a] Quasiclassical transition state theory result. [b] The quasiclassical result including $\Gamma(T)$. [c] The final result based on the transmission coefficient $\gamma(T)$. [d] Experimental, from ref 2.

Table 4: Average Transmission Coefficients and Their Standard Deviation at 298 K

isotope substitution	$\Gamma(T)$	$\kappa(T)$	$\gamma(T)$
HH	0.75 [0.26]	3.13 [1.29]	2.54 [1.61]
DH	0.82 [0.21]	2.88 [0.82]	2.46 [1.09]
HD	0.73 [0.27]	2.84 [1.10]	2.25 [1.45]

average frequencies, as used in previous studies (*37*, *41*, *42*, *68*), or by the direct evaluation of the ratio of the quantum and classical partition functions. We used the AF method for the results presented below.

For the HH case, the inclusion of quantum mechanical vibrational free energy lowers the free energy of activation from the classical mechanical value of 16.1 kcal/mol presented in section 4.1 to 13.6 kcal/mol. These values are denoted (*42*) as quasiclassical (QC) to indicate that the quantization excludes a dynamical degree of freedom, the reaction coordinate, although the final quasiclassical result also includes quasiclassical recrossing. There is no displacement in the location of the transition state from the classical PMF due to the inclusion of quantized vibrations for the HH case. Thus, the quasiclassical transition state corresponds to $z_*^{(1)} = -0.145$ Å. The $k^{(1)}(T)$ column of Table 3 shows the resulting rate constants and free energies of activation.

A total of 13 configurations can be classified as members of the transition state ensemble (TSE) by the criterion explained in section 3.3.2; these configurations are found in the range of $z_*^{(1)}$ from -0.140 to -0.150 Å. For each of these configurations, the primary zone atoms, defined in Figure 5b, were optimized to the nearest saddle point in the presence of the rest of the system (with the rest of the system held fixed), and a minimum energy path (MEP) was obtained. The MEPs were used to determine the individual transmission factors, Γ_i and κ_i, that correct the rate constant for quasiclassical recrossing and multidimensional tunneling, respectively, and the total transmission coefficient, $\gamma(T)$, is obtained by averaging the products of the two individual factors over all the configurations of the TSE. Table 4 shows the computed average transmission coefficients together with their standard deviation. Note that the standard deviation is a characteristic of the fluctuations in the physical system (it is not a measure of any error in the simulations). We note that the standard deviations are larger than those in our previous applications (*37*, *38*, *41*, *68*) of the ensemble-averaged method. The high value of the standard deviation of the transmission coefficients is due to the fluctuations of the individual barrier heights, shapes, and widths for the configurations in a canonical ensemble of transition states. In section 4.4.1, we point out that we have found structures in the transition state region with two possible configurations of the nicotinamide ring with respect to the pterin ring of the substrate. Of the 13 members of the TSE, two belong to one group and 11 belong to the other group. However, this structural difference is not correlated with the values of individual transmission coefficients obtained for the members of each group of configurations.

The final quasiclassical rate constants of this study, $k^{QC}(T)$, are also shown in Table 3; they are the product of the quasiclassical transmission coefficient $\Gamma(T)$ and the quasiclassical transition state theory rate constant $k^{(1)}(T)$. (These results are called quasiclassical because they do not include quantum effects on the motion along the reaction coordinate, although they do include quantization of all other degrees of freedom.) Including quantum mechanical tunneling and quasiclassical dynamical recrossing corrections, our best estimate of the phenomenological free energy of activation and free energy of reaction are 13.1 and -4.7 kcal/mol, respectively, for the hydride transfer step in DHFR. For comparison, the experimental free energy of activation is 13.4 kcal/mol at pH 6.5 (*2*). The final static secondary zone (SSZ) rate constants, $k^{EA-VTST/MT}(T)$, shown in the second last column of Table 3 are the product of the average transmission coefficient, $\gamma(T)$, and the rate constant $k^{(1)}(T)$. They are comparable to the experimental rate constants determined at 298 K and at pH = 6.5 (*2*). Note that the rate constants in the table give an indication of the degree of tunneling. In particular, the fraction of reactions that occur by tunneling F_{tun} is bounded as follows:

$$F_{tun} \geq \frac{k^{EA-VTST/MT} - k^{QC}}{k^{QC}} \qquad (15)$$

The bound would be an equality if there were no nonclassical reflection. Nonclassical reflection reduces the rate (for a typical reaction involving significant amounts of tunneling, nonclasscial reflection might reduce the rate by about by 5−10%; but the tunneling and nonclassical reflection effects are not separated by the numbers in Table 3 because the κ_i factors of eq 9 introduce both effects at the same time). From Table 3, we see that tunneling accounts for more than 71% for the rate constant for the perpriotio case.

4.4. Primary and Secondary Kinetic Isotope Effects. We have determined the primary and secondary KIEs for the hydride transfer reaction catalyzed by DHFR. In these calculations as well as in many other enzymatic reactions, it is essential to include quantum mechanical tunneling contributions in the computed free energy of activation (*25*, *37*, *38*, *41*, *65*, *68*, *74*−*83*). Agarwal et al. (*25*) computed the primary KIE for the hydride transfer reaction in DHFR by means of a mixed quantum/classical description of the nuclei, which includes quantum mechanical effects (such as zero point energy of modes including the transferred atom and hydrogen tunneling) and classical dynamical effects (such as dynamical barrier recrossings) by treating one of the atoms

quantum mechanically. The primary KIE has also been calculated by conventional transition state theory without tunneling based on a single minimized reaction path calculated with a combined QM/MM potential function (*33*). Our study extends the earlier work to both primary and secondary KIEs by using a multidimensional tunneling approach that includes quantal effects on the motion of 40 atoms and that is averaged over an ensemble of 13 transition state configurations.

The inclusion of quantum mechanical vibrational free energy lowers the free energy of activation (16.1 kcal/mol) presented in section 4.1 to 13.6 kcal/mol for the HD substitution (the same value as reported above for the HH case) and to 14.2 kcal/mol for the DH case. The calculated free energy of reaction for the hydride transfer step is −4.7 kcal/mol for all three cases (HH, DH, and HD). As for the HH case, there is no displacement in the location of the transition state from the classical PMF due to the inclusion of quantized vibrations for the HD substitution, which therefore corresponds to $z_*^{QC} = -0.145$ Å. However, for the DH case the maximum of the free energy profile is displaced slightly to $z_*^{QC} = -0.155$ Å. (The $W^{QC}(T,z)$ curve is 8.3×10^{-5} kcal/mol higher at −0.155 Å than at −0.145 Å, a quantitatively insignificant value.) The $k^{(1)}(T)$ column of Table 3 shows how the resulting rate constants and free energies of activation change upon isotopic sustitution. The inclusion of quantum effects on the bound vibrations gives a primary KIE of 2.75 and a secondary KIE of 1.00.

We use the same configurations as the TSE for the three cases, although each isotopic combination engenders its own set of reaction paths and transmission coeeficients. Table 4 shows the computed average transmission coefficients together with their standard deviation for all three isotopic combinations.

The primary and secondary kinetic isotope effects obtained after correcting the rate constant for quasiclassical recrossing by multiplying $k^{(1)}(T)$ by $\Gamma(T)$ are 2.50 and 1.03, respectively. Thus, the inclusion of this correction diminishes the primary KIE and makes a nonnegligible contribution to the secondary KIE. The first fact is explained by a higher quasiclassical transmission coefficient for the DH case than for the HH case, with values 0.82 and 0.75, respectively. Interestingly, these values agree very well with the values 0.85 and 0.80 for the DH and the HH substitution, respectively, obtained by Agarwal et al. (*25*). Thus, both studies (despite having different reaction coordinates) have recrossing corrections of 15−25%. From Table 3 and eq 15, we see that tunneling accounts for more than 67% of the reactive events for the DH case, and more than 68% for the HD case.

We have obtained a final primary KIE of 2.8, in agreement with the experimentally determined value (in the pH range of 5−8) of 3 (*2*), and with the value of 3.2 calculated by Agarwal et al. (*25*). They found that the inclusion of quantum mechanical effects lowers the barrier for the hydride transfer reaction by 2.4 kcal/mol. In comparison, we obtain an overall quantum mechanical correction to the classical free energy of activation of 3.2 kcal/mol (of which 2.5 kcal/mol originates from quantizing nuclear vibration and 0.7 kcal/mol comes from hydrogen tunneling).

Comparing the value obtained for the primary KIE without taking into account dynamical effects on the reaction coordinate (2.7) and the value after the inclusion of the transmission coefficient (2.8) shows that the primary KIE is mainly a consequence of the quantization of bound vibrations. However, the secondary KIE, with a final value of 1.13, is entirely due to dynamical effects on the reaction coordinate, especially tunneling, which contribute a factor of 1.10.

4.5. Analysis of Enzyme−Substrate Interactions. 4.5.1. Hydrogen Bonding Interactions. To shed light on the effect of substrate−enzyme interactions on the enzymatic reaction, we have examined a variety of hydrogen-bonding interactions and their interatomic distances along the reaction path. Since the number of pair interactions is very large, it is impractical to monitor every pair interaction along the reaction pathway. Thus, certain selection criteria were established to facilitate the analysis of key interactions. To begin, from the first umbrella sampling simulations, we focused on three groups of configurations that were generated and saved in the umbrella sampling trajectory, corresponding to the Michaelis complex (the reactant state region defined by the range of $z = z_R \pm 0.250$ Å where $z_R = -1.425$ Å), the transition state (defined by $z = -0.145 \pm 0.100$ Å), and the product state (defined by $z = z_P \pm 0.25$ Å where $z_P = 0.895$ Å). First, we calculated the average distances of all pairs that involve a potential hydrogen bond between a residue of the protein and either the DHF substrate or the NADPH coenzyme or between DHF and NADPH. This resulted in a total of 46 substrate−enzyme, coenzyme−enzyme, and substrate−coenzyme interactions that had donor−acceptor distances of ∼6 Å or less. Then, for analysis with a larger number of configurations, we selected the subset of these interactions that either (i) have donor−acceptor distances that fluctuate by more than 0.2 Å along the reaction or (ii) have been proposed by previous workers (*14*−*16*, *25*, *29*) to be important for catalysis. This subset was analyzed for all 79 400 configurations from the 2 ns of simulations, 9281 in the reactant region, 3411 in the transition state region, and 8966 in the product region; these configurations were used to obtain the averages presented in Table 5. Convergence test with small subsets of the data yielded similar results, indicating that the results are very well converged. The standard deviation for the values in Table 5 is typically 0.001−0.005 Å.

Table 5 also contains coenzyme−enzyme interactions that have been proposed to be important to stabilize the coenzyme in a proper conformation to react with the substrate (*14*). Structural (*14*) and NMR studies (*11*, *12*, *17*) have indicated that the M20 loop that encloses the active site oscillates between different conformational states at a frequency similar to k_{cat}. These conformation states have been classified as the open, closed, and occluded conformations, according to whether the active site is open, closed, or partially closed by the loop. In the reactive form, the closed conformation, of the M20 loop, X-ray crystallographic studies have revealed specific interactions of the M20 loop with the nicotinamide-ribose group of the coenzyme. In addition, the mobile loop forms hydrogen bonds with the F−G loop and helix C, which are characteristic of the closed conformation (*14*). Important interactions that have been identified experimentally are marked by an asterisk in Table 5.

The first four rows of Table 5 show hydrogen bond interactions of either the pteridine ring or the glutamate tail

Table 5: Selected Average Interatomic Distances r_{DA}(Å) between D and A Atoms of the 5-protonated 7,8-dihydrofolate Substrate, the Coenzyme, and the Enzymatic Residues in the Active Center of Dihydrofolate Reductase at Three Points along the Hydride Transfer Reaction[a]

			hydrogen bonds[b]			
	D	A	MC[c]	TS[c]	product	X-ray
DHF-αB	N3	Oδ2, Asp27	2.81	2.80	2.83	2.62
	N2	Oδ1, Asp27	2.90	3.00	2.97	2.97
DHF−RC	NH1, Arg57	O1	2.64	2.63	2.67	2.70
	NH2, Arg57	O2	2.82	2.83	2.85	2.63
DHF−Nic	N8	O7N	3.41	3.61	3.97	3.31
	N5	O7N	4.33	3.72	3.89	3.93
Rib-M20	O2N′	O, Asn18	4.20	3.78	4.02	3.89
	N, Asn18	O3N′	3.21	3.30	3.21	3.43
Nic-M20	N7N*	O, Ile14	2.92	2.95	3.03	3.18
M20-FG	N, Asp122*	O, Gly15	3.28	3.89	3.50	2.95
	N, Glu17*	Oδ1, Asp122	3.52	5.12	5.63	3.13
	N, Glu17*	Oδ2, Asp122	4.03	5.38	5.27	2.77
Rib-FG	O3N′	Oγ1, Thr123	4.71	5.10	4.71	4.18
Pho-αC	NH2, Arg44	O3A′	4.01	3.39	3.00	4.19
	Nε, Arg44	O2A′	3.47	3.38	3.20	3.93
	O3PA	Nε, Arg44	3.48	3.30	3.42	3.67
Pho-CD	N, Ser64	O1PA	2.69	2.68	2.73	2.77
	N, Gln65	O1PA	3.82	3.72	3.75	4.37

	other interactions	MC	TS	product	X-ray
C11	Cζ, Phe31	5.44	5.14	5.13	5.18
Cδ, Ile14	OH, Tyr100	5.28	5.07	5.09	5.45
C4N	OH, Tyr100	3.75	3.58	3.80	2.98
C3N′*	O, Asn18	4.73	4.04	4.26	4.46

[a] An asterisk denotes an important interaction that has been identified experimentally. See Figure 2 for a key to atomic labels. [b] In the case of hydrogen bonds, D is the proton donor and A is the proton acceptor. [c] MC and TS stand for Michaelis complex and transition state, respectively. The distances found in the X-ray structure with PDB code 1RX2 are in the last column of the table.

of the substrate with enzymatic residues in the B helix or in a random coil (RC) connecting the seventh β-sheet with helix C. These interactions show little variation in going from the Michaelis complex through the transition state to the product and are maintained throughout the simulation, a feature found by other groups (*29*−*31*). These interactions are responsible for the polarization of the substrate in the active center of DHFR enzyme (*29*, *31*). In a separate paper (*31*), we have presented a quantitative determination of the energetic consequences of this polarization effect.

The fifth and sixth rows of Table 5 show strong interactions between the pteridine ring of the 5-protonated 7,8-dihydrofolate substrate and the nicotinamide ring. Evidently, the carbonyl oxygen (O7N) of the nicotinamide ring interacts predominantly with the N8 atom of the substrate in the Michaelis complex (interaction distance is 3.41 Å), while the interaction with the N5 atom is weaker (the interaction distance is 4.33 Å). However, the latter interaction becomes stronger at the transition state and the product geometry with significantly shortened distances of 3.72 and 3.89 Å, respectively. This is accompanied by a decrease in the distance between N8 and O7N atoms at the two critical points along the reaction path (3.61 and 3.97 Å, respectively). Further analysis shows that these shortened distances at the transition state and in the product result from two different possible orientations of the nicotinamide ring with respect to the substrate, which depend on the substrate atom (N5 or N8) that interacts with the carbonyl oxygen (O7N) of the nicotinamide ring.

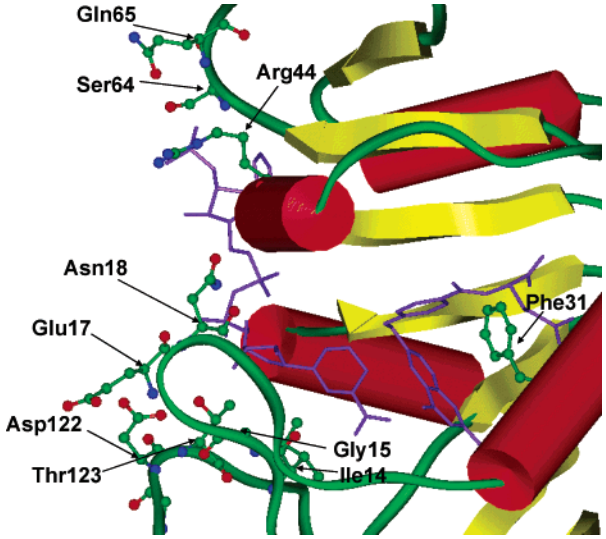

FIGURE 7: Partial view of the DHF−NADPH−DHFR complex. The residues that are cited in the text (section 4.2.1) because they interact with the coenzyme through hydrogen bond interactions are represented in ball-and-stick model.

The remaining hydrogen bond distances in Table 5 correspond to interaction between residues and substrate atoms involving the nicotinamide (Nic), ribose (Rib), or phosphate (Pho) components of the coenzyme, the M20 loop (Asn18, Ile14, Gly15, Glu17), the CD loop (Ser64, Gln65), the FG loop (Asp122, Thr123), and helix C (Arg 44) (see Figures 1 and 7). In going from the reactant to the transition state, the M20 loop residues move closer to the coenzyme, whereas the interaction between the FG loop and either of the coenzyme and the M20 loop decreases. This suggests that the M20 loop stabilizes the transition state, in agreement with experimental findings (*84*). The next section (4.4.2) presents an electrostatic energy analysis that is consistent with this conclusion based on distances. Table 5 also indicates that the interactions between Arg44 and the coenzyme are reinforced at the transition state.

Finally, the last four rows of Table 5 give results for four interactions that have been discussed in previous studies (*24*−*28*). Our simulation shows that Phe31 (see Figure 7) and the *p*-ABA ring of the substrate move closer by about 0.3 Å as the hydride transfer reaction occurs, as do residues Ile14 and Tyr100. Similar findings have been noted by Agarwal et al. (*24*). The shortening of the distance between the side chain of Tyr100 and the donor atom C4N suggests that this residue may provide electrostatic stabilization of the transition state. The same inference may be drawn from the van der Waals contact between the backbone oxygen of the M20 loop residue Asn18 and the NC3′ atom of the ribose ring of the coenzyme.

The correlation of characteristic structural changes, especially hydrogen bond distances, along the hydride transfer reaction path in DHFR has been described as coupled promoting motions that provide stabilization to the transition state by Agarwal et al. (*24*, *25*). Although these authors have been careful in defining the meaning of "promoting motions", it perhaps should be emphasized again that the changes in hydrogen bonding distances are results of thermodynamic averages of conformational substates of the enzyme in its reactant, transition state, and product region. These "motions" are not dynamically correlated in real time with the hydride

transfer motion. They actually occur on a much slower time scale, but the umbrella sampling algorithm shows that they are correlated geometrically. That is, when the reaction coordinate is near the transition state, these average hydrogen bond distances may tend to be larger or smaller than they are when the reaction coordinate is in the reactant region. Changes in average protein conformations and ligand coordination from the Michaelis complex to the transition state and finally to the product state have been observed experimentally (*14*, *85*−*87*) and computationally (*23*, *25*, *41*, *88*, *89*) for many enzyme systems, and the contribution of protein conformational free energy to catalysis has been estimated for the reaction catalyzed by orotidine monophosphate decarboxylase (*89*).

The present study of the DHFR reaction shows similar variations in hydrogen bond distances and in the Phe31−C11 distance to those reported by Agarwal et al. (*24*, *25*). The agreement in these variations is particularly pleasing because different computational approaches have been used, including the potential energy surface and the definition of the reaction coordinate.

It would be interesting to determine the energetic contributions of the structural changes to catalysis.

4.5.2. Differential Interactions along the Reaction Path. The change of hydrogen bond distances discussed above provides a qualitative indication that these residues may be involved in the stabilization or destabilization of the transition state in the chemical step. To identify their functional roles, we have carried out an interaction energy decomposition analysis using the combined QM/MM potential at the reactant state, transition state, and product state. (The SVB term in the QM(AM1-SVB)/MM potential affects the configurations generated in the MD simulation but does not affect this electrostatic analysis.) This approach was first used by Bash et al. (*90*) for the enzyme triosephosphate isomerase, and it involves sequentially annihilating the partial charges of amino acid residues, starting from the ones closest to the substrate. Although the specified contributions from individual residues to the overall protein−substrate interaction depend on the order of the charge annihilation, the results do provide a reasonable estimate of the magnitude of the interaction energy and a good indication of the role of each residue in stabilizing or destabilizing the transition state (*91*).

In combined QM/MM calculations, the total potential energy of the system is expressed as follows:

$$V_{QM/MM} = E_{QM} + E_{QM/MM} + E_{MM} \qquad (16)$$

where E_{QM} is the internal energy of the subsystem treated by QM in the presence of the protein−solvent environment, $E_{QM/MM}$ represents the interaction energy between the QM and MM region, which is the sum of electrostatic contributions from interactions of the QM subsystem with all MM residues and water molecules in the system as well as with the MM parts of the substrate and coenzyme, and E_{MM} is the total energy (Coulomb and van der Waals) of the MM subsystem plus the van der Waals interactions between the QM and MM subsystems. The first two terms in eq 16 are computed using the QM electronic structural method, which is the semiempirical AM1 model in the present study. In the energy decomposition analysis presented in this section, the term "quantum mechanical electrostatic energy" refers to the sum of the first two terms in eq 15. An important feature of combined QM/MM calculations is that the electronic polarization of the QM subsystem by its environment is naturally included in eq 16 by the self-consistent-field optimization of the wave function.

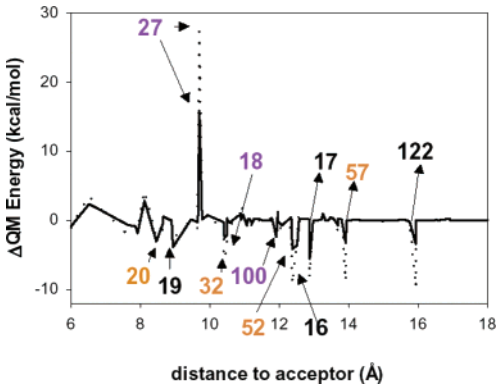

FIGURE 8: Individual residue contribution to stabilize or destabilize the transition state (solid line) and product (dotted line) with respect to the reactant as a function of the distance between the C_α atom of the residue and the C6 atom of the substrate. The residue numbers of the residues with largest magnitude contributions are indicated. Numbers in orange indicate residues that interact with the substrate, and numbers in violet indicate residues that interact with the coenzyme.

From the molecular dynamics configurations saved in the forward umbrella sampling simulation, we selected all configurations with a value of z within 0.1 Å of the reactant, product, or transition state, corresponding to $z_R = -1.425$ Å, $z_P = 0.895$ Å, and $z_* = -0.145$ Å, respectively. For each configuration, we have sequentially zeroed the MM charges of the enzymatic residues in order of the shortest distance between the C_α atom and the C6 atom of the substrate DHF. At each deletion step, the difference in quantum mechanical electrostatic energy before and after the charge annihilation is defined as the interaction energy of this residue, I, with the QM subsystem.

$$\Delta E(I) = [E_{QM}(I) - E_{QM}(I-1)] + [E_{QM/MM}(I) + E_{QM/MM}(I-1)] \qquad (17)$$

The final results are averaged over all the reactant, product, and transition state configurations, respectively. To shed light on the importance of each residue during the hydride transfer reaction, relative interaction energies at the transition state and product are obtained by subtracting the interaction energies in the reactant state; these differences of the average TS or product value from the average reactant values are shown in Figure 8. Figure 9 shows a snapshot of the active site that illustrates interactions of residues having significant contributions.

At first glance, Figure 8 shows that the overall transition/product state stabilization comes from contributions of many residues at distances ranging from 8 to 16 Å from the reaction center. An interesting observation is that the same residues that stabilize the transition state also stabilize the product, but the effect is generally greater for the product. Most interactions that have significant changes in going from the reactant state to the transition state provide a stabilizing effect. The only exception is Asp27, which is directly hydrogen bonded to two nitrogen atoms of the pteridine ring,

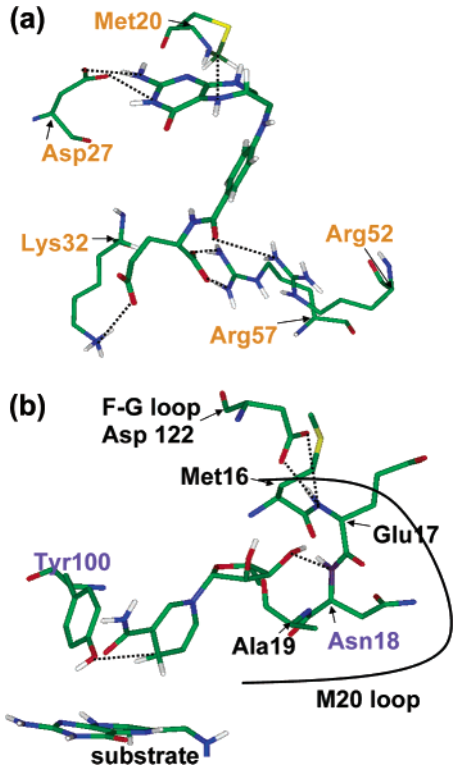

FIGURE 9: Snapshot of the reactant state showing (a) interactions between the substrate and the enzymatic residues with highest individual electrostatic interaction in Figure 8, and (b) interactions between the nicotinamide and ribose rings of the coenzyme and the enzymatic residues with highest individual electrostatic interaction in Figure 8. In panel b, the solid black curve shows the trace of the M20 loop by surrounding the M20 loop residues that are shown in the figure.

but destabilizes the transition state and the product by 13 and 28 kcal/mol, respectively. This is due to the hydride transfer reaction, resulting in a net increase in negative charge density on the substrate. Interestingly, Table 5 shows that the hydrogen bond distance between Asp27 and the N3 and N2 atoms of the substrate hardly changes along the reaction path, suggesting that examining geometrical features alone can be misleading for inferring the mechanism of enzymatic reactions. In fact, it is useful to consider both the variation in hydrogen bond distances and their correlation with interaction energy.

The destabilizing effect of Asp27 is surprising in its magnitude, although not unprecedented (*92*), and it is compensated by stabilizing interactions between the substrate and other residues, including Met20, Lys32, Arg52, and Arg57, through direct hydrogen bonding and long-range electrostatic interactions (Figures 8 and 9a). The Cϵ atom of Met20 is within van der Waals contact distance (3.92, 4.24, and 3.8 Å at the reactant, TS, and product, respectively) of the N5 atom of the substrate, and Arg57 is hydrogen bonded to two carboxylate oxygens of the glutamate tail (see Table 5). Lys32 and Arg52 are more than 5 Å away from the substrate, and thus their effect is due to long-range electrostatics. These two residues, together with Arg57, have been proposed to polarize the substrate, but this proposal has not been quantitatively demonstrated (*29*). In a separate study (*31*), we have determined the total polarization effect of the enzyme on the product tetrahydrofolate, and we found that it accounts for 3.5% of the total electrostatic interaction energy, and it amounts to −19.3 (±0.5) kcal/mol.

Of the residues that stabilize the transition state in Figure 8, Tyr100 and Asn18 directly interact with the coenzyme (Figure 9b), and their stabilization effect is mirrored by a decrease in hydrogen bond distances in Table 5. Three residues in the M20 loop, Met16, Glu17, and Ala19, are found to stabilize the TS, although they are not hydrogen bonded to the substrate or coenzyme. Li et al. (*84*) found that replacing residues 16−19 of the M20 loop by a single glycine results in a decrease in the rate of the hydride transfer step from 950 to 1.7 s^{-1}. Our computational experiment is consistent with these mutagenesis studies. The distant residue Asp122 in the FG loop (16 Å from the C6 atom) stabilizes the transition state and the product by 3.5 and 10.0 kcal/mol, respectively. The FG loop affects the substrate and coenzyme through hydrogen-bonding interactions with the M20 loop. Table 5 shows that as the M20 loop closes in to form stronger hydrogen bonds at the transition state, the FG loop residue Asp122 increases its distance from the M20 loop and the substrate. The stabilizing effect of Asp122 is probably due to the increase of positive charge on the nicotinamide moiety of the coenzyme.

The total QM/MM electrostatic interaction energy between the enzyme and the substrate and coenzyme was found to increase in going from the reactant to the transition state, and the difference is very large, including 9 kcal/mol due to electronic polarization of the QM region (*31*). Overall, our results indicate that the electrostatic stabilization of the transition state plays an important role in the reaction of DHFR.

Zhu et al. (*93*) have synthesized a series of 1-aryl-1,4-dihydronicotinamides as NAD(P)H models, and they have determined the second-order rate constants for oxidation by 2-methyl-5-nitroisoquinolinium cation in aqueous solution. The phenomenological free energy of activation corresponding to the measured reaction rates is about 19 kcal/mol, which is about 6 kcal/mol higher than the free energy of activation for the enzymatic hydride transfer reaction. This provides an estimation of the catalytic effect on the chemical step of changing the surrounding medium from water to enzyme, coenzyme, and water, and it would be interesting to try to relate this observation to the kind of calculations presented here.

4.6. Comparison of Two Reaction Coordinates. As mentioned above, DHFR has been studied with two types of reaction coordinates. In the present study, the reaction coordinate, *z*, of stage 1 of the calculation is defined in terms of two bond distances, eq 14, and the umbrella sampling technique is used to drive the enzymatic system from the reactant complex to the transition state and product complexes. Experience with this approach seems to indicate that it can provide adequate sampling of the environmental configurations (*38*, *41*). Another widely used way of defining the reaction coordinate, with its origins in electron transfer theory, is to use the energy or polarization difference between reactant and product diabatic states to gauge the progress of the reaction (*94*−*105*), for example:

$$\Delta E = V_R - V_P \tag{18}$$

where V_R and V_P are, respectively, the energy of the diabatic

reactant state and the diabatic product state. Because the energies of the diabatic states include not only solute internal energies but also solute−solvent interaction energies, this kind of ΔE is a collective reaction coordinate that includes a physical combination of solvent coordinates. In the present approach, the solvent and the secondary-zone part of the protein participate in the reaction coordinate only in stage 2, where the use of different reaction coordinates for different solvent configurations incorporates the solvent into an effective reaction coordinate. The hydride transfer reaction in DHFR has been studied by using the energy gap reaction coordinate ΔE by Agarwal et al. (*25*). In their study, the ground state potential energy surface was modeled empirically by an empirical valence bond (EVB) potential (*98*) that included two structures that mimic the reactant and product state, respectively, and the diagonal elements, V_R and V_P, were described by the GROMOS force field (*106*), except that (see below) certain van der Waals interactions were omitted, and Morse potentials were used for the bonds between the transferring hydride and the donor (or acceptor) carbon atom for the diabatic state 1 (or 2). (In contrast, as stated above, we used a QM/MM potential rather than EVB and the CHARMM22 force field rather than GROMOS.)

In the approaches that use a geometric reaction coordinate, the solvent must respond to the changes in the solute internal degrees of freedom along the reaction coordinate, while both solvent and solute must respond to the bias of the energy gap potential in simulations employing eq 18 as the control variable. The two approaches have been compared in detail elsewhere (*100*, *103*, *105*). A key issue is that the potential of mean force is evaluated as a function of the reaction coordinate. Consequently, the quasithermodynamic free energy of activation depends on the choice of the reaction coordinate, although the estimated rate constant would be the same if an accurate transmission coefficient were included in both approaches. In some publications (*97*, *100*), it has been suggested that the use of only solute geometrical parameters to define the reaction coordinate for reactions in solution will not provide adequate sampling of the solvent/protein configurations. However, other studies have led to different conclusions (*38*, *41*, *103*, *105*), and the efficiency of solvent configuration sampling in simulations that employ a solute reaction coordinate has not been directly assessed. Here we examine this question by directly evaluating the distribution of values of a collective solvent reaction coordinate for the configurations sampled in simulations driven by a geometric solute reaction coordinate. If the criticism were indeed true, one might expect that a gap will be evident in the distribution of solvent reaction coordinate values when one proceeds from reactants to products using enzyme configurations sampled by the solute reaction coordinate.

To analyze the sampling efficiency of the energy-gap reaction coordinate in simulations based on a geometrical reaction coordinate, we have computed the energy gap, ΔE, for all 7200 structures that were saved during the first umbrella sampling simulation. In these calculations, the diabatic state potential energies V_R and V_P were defined as in ref 25 and were calculated using the CHARMM22 force field (*48*), except that, as in ref 25, the van der Waals parameters for the interactions of the transferring hydride atom with the acceptor atom, the donor atom, or the other

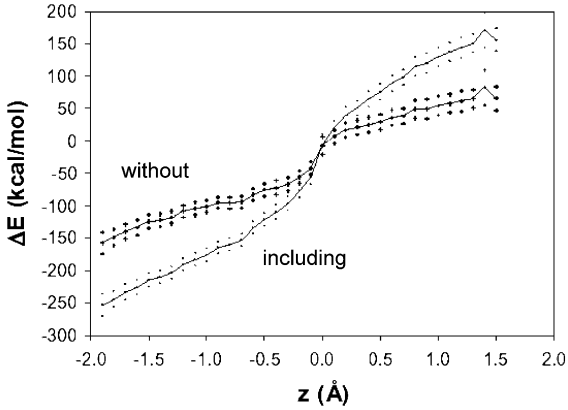

FIGURE 10: Energy gap reaction coordinate calculated including the Morse potential for the C−H4 bond (dotted symbols) or without including it (crosshair symbols) as a function of the geometric reaction coordinate used to study the hydride transfer reaction in DHFR. For both cases, the solid curve connects the average values over bins of width 0.1 Å, and the symbols above or below are the result of adding or subtracting the corresponding standard deviation.

hydrogen atom on the donor carbon C4N, have been set to zero, and a Morse potential was used for the bond terms C4N−H4 and C6−H4 in V_R and V_P, respectively. The Morse potentials are given by

$$M(R_{CH}) = D_{CH}(1 - e^{-\alpha(R_{CH}-R_e)})^2 \qquad (19)$$

where R_{CH} is the distance between the hydride and the bonded donor or acceptor carbon atom, D_{CH} is the dissociation energy of the C−H bond, R_e is the equilibrium bond distance between atoms C and H, and α is the range parameter related to the force constant k_{CH} and the bond dissociation energy by $\alpha = (k_{CH}/2D_{CH})^{1/2}$. All the parameters in eq 19 were taken from ref 25. Since valence bond states V_R and V_P have been defined by a molecular mechanics force field, the charges on all the atoms are fixed for a given valence bond state, and they represent the polarization of the atoms in the system at the reactant or at the product, respectively. The charges on the atoms that were represented as quantum mechanical atoms in the QM(AM1-SVB)/MM simulations carried out to calculate the PMF and to generate the configurations used to determine $\Delta E(z)$, have been taken from the average values obtained during two 10 ps molecular dynamics simulations at the reactant and at the product states, respectively. To avoid charge transfer between the fragments (pterin ring and nicotinamide ring), we developed charges for the fragments in each VB state using single-point QM/MM calculations where only one of the two fragments was represented quantum mechanically. (Additional tests showed that the results do not depend significantly on this restriction of charge transfer.)

The average of eq 18 over bins of width 0.1 Å gives the function $\Delta E(z)$, which is plotted in Figure 10. Figure 10 shows that the configurations sampled using the geometric reaction coordinate include the full range of values of the energy gap coordinate. Furthermore, this is still true when we remove the Morse term that represents the change in the intramolecular interactions of the solute in going from reactants to products (curve with crosshair symbols in Figure 10). Therefore, umbrella sampling calculations that employ a geometric reaction coordinate can provide solvent/protein configurations that span the same range of solute−solvent

Table 6: CHARMM Topology File Associated with the 5-Protonated DHF Molecule and the Nicotinamide and Ribose Rings of the NADPH Molecule and CHARMM Parameter File Associated to the 5-Protonated DHF Molecule

```
RESI QMP −1.08
! DHF molecule
GROUP PTERIN
ATOM   N1 NN3G   −0.34280
ATOM   C2 CN2     0.33045
ATOM   NA2 NN1   −0.31652
ATOM   HA21 HN1   0.32769
ATOM   HA22 HN1   0.26521
ATOM   N3 NN2G   −0.32320
ATOM   H3 HN2     0.34085
ATOM   C4 CN1     0.41298
ATOM   O4 ON1    −0.43951
ATOM   C4A CN5G  −0.36937
ATOM   N5 NN2     0.08607
ATOM   HP HN2     0.34746
ATOM   C6 CA     −0.04909
ATOM   C7 CT2    −0.00273
ATOM   H71 HA     0.10860
ATOM   H72 HA     0.14338
ATOM   N8 NN2    −0.29864
ATOM   H8 HN2     0.28209
ATOM   C8A CN5    0.30777
GROUP pABA
ATOM   C9 CT2     0.02198
ATOM   H91 HA     0.15452
ATOM   H92 HA     0.10156
ATOM   N10 NH1   −0.33883
ATOM   H10 H      0.28444
ATOM   C11 CA    −0.18192
ATOM   C12 CA    −0.02821
ATOM   H12 HP     0.15231
ATOM   C13 CA    −0.19923
ATOM   H13 HP     0.16268
ATOM   C14 CA     0.12150
ATOM   C15 CA    −0.24807
ATOM   H15 HP     0.12424
ATOM   C16 CA    −0.04124
ATOM   H16 HP     0.13025
ATOM   C C        0.39306
ATOM   O O       −0.48595
ATOM   N NH1     −0.34668
ATOM   H H        0.25183
GROUP GLU
ATOM   HA HB      0.0900
ATOM   CB CT2    −0.1800
ATOM   HB1 HA     0.0900
ATOM   HB2 HA     0.0900
ATOM   CG CT2    −0.2800
ATOM   HG1 HA     0.0900
ATOM   HG2 HA     0.0900
ATOM   D CC       0.6200
ATOM   OE1 OC    −0.7600
ATOM   OE2 OC    −0.7600
ATOM   CT CC      0.6200
ATOM   O1 OC     −0.7600
ATOM   O2 OC     −0.7600
! NADPH molecule (nicotinamide and ribose)
GROUP NICO
ATOM   NC2′ CN7B −0.03355
ATOM   NH2′ HN7   0.13045
ATOM   NO2′ ON5  −0.32069
ATOM   NH2T HN5   .23741
ATOM   NC3′ CN7  −0.03629
ATOM   NH3′ HN7   0.11196
ATOM   NO3′ ON5  −0.36248
ATOM   NH3T HN5   .22359
ATOM   NC1′ CN7B  0.11554
ATOM   NH1′ HN7   0.10965
ATOM   NC4′ CN7   0.01349
ATOM   NH4′ HN7   0.17032
ATOM   NO4′ ON6B −0.25622
ATOM   NN1 NN2   −0.21681
ATOM   NC6 CN3C  −0.03237
ATOM   NH6 HN6    0.18652
ATOM   NC5 CN3   −0.24761
ATOM   NH5 HN6    0.16108
ATOM   NC4 CN8   −0.04350
ATOM   NH4 HN8    0.08494
ATOM   NH42 HN8   0.07656
ATOM   NC3 CN3   −0.29826
ATOM   NC2 CN3C   0.05753
ATOM   NH2 HN6    0.16789
ATOM   NC7 CN1A   0.36143
ATOM   NO7 ON1   −0.44747
ATOM   NN7 NN1   −0.42416
ATOM   NH71 HN1   0.23400
ATOM   NH72 HN1   0.21663
!boundary atom
ATOM   NC5′ CN8B −0.01824
GROUP BOUND
ATOM   CA CT1    −0.03027
```

CHARMM parameter file associated to the 5-protonated DHF molecule

```
BONDS
CA C        250.0    1.4900
NH1 CA      370.0    1.3450
NN2 CA      370.0    1.4800
NN2 CT2     370.0    1.3200
CN5G NN2    370.0    1.4000
NN2 CT1     370.0    1.4500
ANGLES
O C CA       80.0    118.00
NH1 C CA     80.0    118.00
CN1 CN5G NN2 70.0    120.59
NN2 CN5G CN5 70.0    119.95
CN5G NN2 CA  70.0    121.87
NN2 CA CT2   70.0    121.95
CT2 CA CT2   70.0    115.88
CA CT2 NN2   70.0    114.00
CT2 NN2 CN5  70.0    120.02
NN3G CN5 NN2 70.0    116.75
CN5G CN5 NN2 70.0    120.71
CA CT2 NH1   70.0    110.15
CT2 NH1 CA   70.0    109.00
NH1 CA CA    70.0    116.00
CA CA C      70.0    117.00
CN5G NN2 HN2 70.0    117.84
HN2 NN2 CA   70.0    120.30
HA CT2 NN2   70.0    107.83
CT2 NN2 HN2  70.0    116.72
H NH1 CA     70.0    107.06
DIHEDRALS
H NH1 C CA      2.5   2   180.00
CT1 NH1 C CA    2.5   2   180.00
CN1 CN5G NN2 CA 2.5   2   181.85
CN5G NN2 CA CT2 2.5   1     0.07
CA NN2 CN5G CN5 2.5   1     2.43
CA CT2 NN2 CN5  2.5   1    13.32
CA CT2 NH1 CA   2.5   1    73.19
CT2 NH1 CA CA   2.5   2   177.67
NH1 CA CA CA    2.5   2   179.67
CA CA C O       2.5   1     0.00
CA CA C NH1     2.5   2   159.18
CA CA CA C      2.5   2   180.00
CN1 CN5G NN2 HN2 2.5  1     0.00
HN2 NN2 CN5G CN5 2.5  2   180.00
HN2 NN2 CA CT2  2.5   2   180.00
CA CT2 NN2 HN2  2.5   2   180.00
CA CT2 NH1 H    2.5   1   −50.00
HA CT2 NN2 CN5  2.5   1   134.86
HA CT2 NN2 HN2  2.5   1   −64.16
HA CT2 NH1 CA   2.5   1   −163.22
NH1 CA CA HP    2.5   1   −0.28
H NH1 CA CA     2.5   1   −61.88
HP CA CA C      2.5   1     0.00
```

interaction energies as that in simulations using an energy-gap mapping potential (reaction coordinate). Our analysis shows no particular advantage of using the energy-gap reaction coordinate over the geometrical reaction coordinate, at least with regard to sampling efficiency of the enzyme conformational subspace as measured by the range of protein−substrate interactions. Nevertheless, the representation of the potential of mean force as a function of the

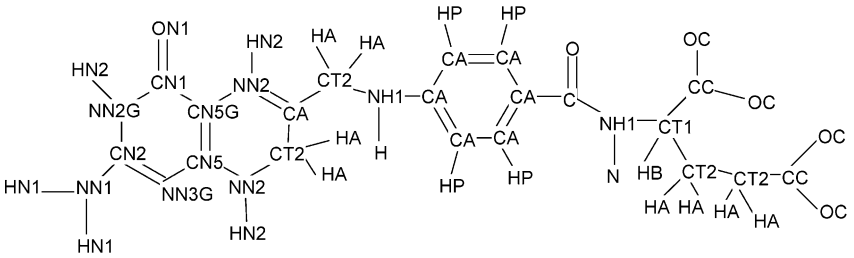

FIGURE 11: Schematic representation of the 5-protonated DHF molecule with the atom type assigned to each atom.

energy-gap reaction coordinate provides a different perspective on the reaction mechanism than is provided by the geometrical reaction coordinate. Furthermore, one reaction coordinate would be much better than the other if one of them has a significanly smaller value of the recrossing transmission coefficient Γ. However, previous estimates of the transmission coefficients for enzymatic reactions, for either type of reaction coordinate, are close to unity (*25*−*27*, *37*, *38*, *41*, *68*, *104*, *107*), and for DHFR and LADH (*26*, *37*) the values of Γ computed by the two approaches are very similar. In these circumstances, the computed free energies of activation are expected to be similar from geometrical or energy-gap reaction coordinates, if one uses the same PES. Furthermore, as discussed above, good agreement was obtained between structural (section 4.4.1) and kinetic (sections 4.3 and 4.4) results obtained by using the two different approaches.

5. CONCLUDING REMARKS

The results obtained in the present study provide further insight into the catalysis of the hydride transfer reaction from NADPH to 5-protonated DHF by the enzyme dihydrofolate reductase. Starting with structures of the enzyme, substrate, and cofactor, we carried out molecular dynamics simulations with periodic boundary conditions based on a combined QM/MM (*34*−*36*) potential energy surface. The molecular dynamics simulations start with classical trajectories involving 21 468 atoms, and then quantum mechanical effects are incorporated on the dynamics of 120 degrees of freedom. These simulations provide many molecular-level details that are inaccessible to experiment. We have obtained the free energy profile for the hydride transfer reaction as a function of a reaction coordinate that depends on geometrical parameters of the reactants, and we ascertained that, although tunneling makes only a small change in the primary kinetic isotope effect, it makes a large change in the secondary kinetic isotope effect. We have determined the relative stabilization afforded by individual enzymatic residues to the transition state and to the product state with respect to the reactants. Furthermore, the variation of key hydrogen bond distances along the reaction path has been investigated and compared to similar results obtained by Agarwal et al. (*25*) using a different reaction coordinate, in particular an energy gap coordinate, which is the difference in energy between reactant and product diabatic states defined by molecular mechanics. Good agreement was obtained for both structural and kinetic results obtained by the two approaches, in contrast to the view (*100*) that a geometric coordinate is not able to properly sample the transition state region. This encouraged us to carry out a comparative study of both coordinates, which further confirmed the usefulness of the geometrical coordinate.

We have calculated the primary and secondary KIEs using ensemble-averaged variational transition state theory with multidimensional tunneling (*37*, *38*) (EA-VTST/MT). Our study, in agreement with previous results obtained by Agarwal et al. (*25*), demonstrates that quantum mechanical vibrational effects are important for computing the potential of mean force of the reaction because they lower the barrier height by ∼3 kcal/mol, and that it is essential to incorporate multidimensional quantum tunneling contributions to estimate the primary kinetic isotope effects for the hydride transfer reaction. Our calculation of the secondary kinetic isotope effect is the first such calculation for DHFR, and we predict a kinetic isotope effect of 1.13, mainly due to tunneling.

NOTE AFTER ASAP POSTING

This article posted on the ASAP website on October 21, 2003 contained two errors. The Glu20 label in Figure 3 should have been Glu17, and the title to Table 6 was incomplete. This information has been corrected in this new version posted October 29, 2003.

APPENDIX

The CHARMM topology file associated with the 5-protonated DHF molecule and the nicotinamide and ribose rings of the NADPH molecule is shown in Table 6. The atom types assigned to each atom of the 5-protonated DHF molecule are indicated in Figure 11. The atom types for the atoms of the NADPH molecule were taken from the standard definition in the CHARMM topology file. The charges for all the atoms in the groups PTERIN, pABA, NICO, and BOUND were obtained from a QM/MM single point calculation with these atoms represented quantum mechanically at the AM1 semiempirical level of theory and the rest of the substrate and coenzyme atoms, the protein atoms, and the solvent described by the CHARMM22 force field. The charges for the atoms in the GLU group are the standard CHARMM22 charges for a glutamate residue.

REFERENCES

1. Blakley, R. L. (1995) *Adv. Enzymol. 70*, 23.
2. Fierke, C. A., Johnson, K. A., and Benkovic, S. J. (1987) *Biochemistry 26*, 4085.
3. Morrison, J. F., and Stone, S. R. (1988) *Biochemistry 27*, 5499.
4. McTigue, M. A., Davies, J. F., II, Kaufman, B. T., and Kraut, J. (1992) *Biochemistry 31*, 7264.
5. Chen, Y.-Q., Kraut, J., Blakley, R. L., and Callender, R. (1994) *Biochemistry 33*, 7021.
6. Lee, H., Reyes, V. M., and Kraut, J. (1996) *Biochemistry 35*, 7012.
7. Deng, H., and Callender, R. (1998) *J. Am. Chem. Soc. 120*, 7730.
8. Cannon, W. R., Garrison, B. J., and Benkovic, S. J. (1997) *J. Am. Chem. Soc. 119*, 2386.

9. Cummins, P. L., and Gready, J. E. (2001) *J. Am. Chem. Soc. 123*, 3418.
10. Shrimpton, P., and Allemann, R. K. (2002) *Protein Sci. 11*, 1442.
11. Falzone, C. J., Wright, P. E., and Benkovic, S. J. (1994) *Biochemistry 33*, 439.
12. Epstein, D. M., Benkovic, S. J., and Wright, P. E. (1995) *Biochemistry 34*, 11037.
13. Cameron, C. E., and Benkovic, S. J. (1997) *Biochemistry 36*, 15792.
14. Sawaya, M. R., and Kraut, J. (1997) *Biochemistry 36*, 586.
15. Miller, G. P., and Benkovic, S. J. (1998) *Biochemistry 37*, 6327.
16. Miller, G. P., and Benkovic, S. J. (1998) *Biochemistry 37*, 6336.
17. Osborne, M. J., Schnell, J., Benkovic, S. J., Dyson, H. J., and Wright, P. E. (2001) *Biochemistry 40*, 9846.
18. Miller, G. P., Wahnon, D. C., and Benkovic, S. J. (2001) *Biochemistry 40*, 867.
19. Appleman, J. R., Beard, W. A., Delcamp, T. J., Prendergast, N. J., Freisheim, J. H., and Blakeley, R. A. (1990) *J. Biol. Chem. 265*, 2740.
20. Rajagopalan, P. T. R., and Benkovic, S. J. (2002) *Chem. Rec. 2*, 24.
21. Huang, Z., Wagner, C. R., and Benkovic, S. J. (1994) *Biochemistry 33*, 11576. Wagner, C. R., Huang, Z., Singleton, S. F., and Benkovic, S. J. (1995) *Biochemistry 34*, 15671.
22. Rajagopalan, P. T. R., Lutz, S., and Benkovic, S. J. (2002) *Biochemistry 41*, 12618.
23. Radkiewicz, J. L., and Brooks, C. L., III. (2000) *J. Am. Chem. Soc. 122*, 225.
24. Agarwal, P. K., Billeter, S. R., Rajagopalan, P. T. R., Benkovic, S. J., and Hammes-Schiffer, S. (2002) *Proc. Natl. Acad. Sci. U.S.A. 99*, 2794.
25. Agarwal, P. K., Billeter, S. R., and Hammes-Schiffer, S. (2002) *J. Phys. Chem. B 106*, 3283.
26. Hammes-Schiffer, S. (2002) *Biochemistry 41*, 13335.
27. Watney, J. B., Agarwal, P. K., and Hammes-Schiffer, S. (2003) *J. Am. Chem. Soc. 125*, 3745.
28. Thorpe, I. F., and Brooks, C. L., III, personal communication.
29. Bajorath, J., Kraut, J., Li, Z., Kitson, D. H., and Hagler, A. T. (1991) *Proc. Natl. Acad. Sci. U.S.A. 88*, 6423.
30. Greatbanks, S. P., Gready, J. E., Limaye, A. C., and Rendell, A. P. (2000) *J. Comput. Chem. 21*, 788.
31. Garcia-Viloca, M., Truhlar, D. G., and Gao, J. (2003) *J. Mol. Biol. 327*, 549.
32. Cummins, P. L., and Gready, J. E. (1998) *J. Comput. Chem. 19*, 977.
33. Castillo, R., Andres, J., and Moliner, V. (1999) *J. Am. Chem. Soc. 121*, 12140.
34. Field, M. J., Bash, P. A., and Karplus, M. (1990) *J. Comput. Chem. 11*, 700.
35. Gao, J. (1995) in *Rev. Comput. Chem.* (Lipkowitz, K. B., Boyd, D. B., Eds.) Vol. 7, p 119, VCH, New York.
36. Gao, J., Amara, P., Alhambra, C., and Field, M. J. (1998) *J. Phys. Chem. A 102*, 4714.
37. Alhambra, C., Corchado, J. C., Sanchez, M. L., Garcia-Viloca, M., Gao, J., and Truhlar, D. G. (2001) *J. Phys. Chem. B 105*, 11326.
38. Truhlar, D. G., Gao, J., Alhambra, C., Garcia-Viloca, M., Corchado, J. C., Sánchez, M. L., and Villà, J. (2002) *Acc. Chem. Res. 35*, 341.
39. Cook, P. F., Ed. (1991) *Enzyme Mechanism from Isotope Effects*, CRC Press, Boca Raton, FL.
40. Devi-Kesavan, L. S., Garcia-Viloca, M., and Gao, J. (2003) *Theor. Chem. Acc. 109*, 133.
41. Garcia-Viloca, M., Alhambra, C., Truhlar, D. G., and Gao, J. (2003) *J. Comput. Chem. 24*, 177.
42. Garcia-Viloca, M., Alhambra, C., Truhlar, D. G., and Gao, J. (2001) *J. Chem. Phys. 114*, 9953.
43. Truhlar, D. G., Isaacson, A. D., and Garrett, B. C. (1985) in *Theory of Chemical Reaction Dynamics* (Baer, M., Ed.) Vol. 4, p 65, CRC Press: Boca Raton.
44. Anderson, J. B. (1995) *Adv. Chem. Phys. 91*, 381.
45. Liu, Y.-P., Lynch, G. C., Truong, T. N., Lu, D. H., Truhlar, D. G., and Garrett, B. (1993) C. *J. Am. Chem. Soc. 115*, 2408.
46. (a) Liu, Y.-P., Lu, D.-h., Gonzalez-Lafont, A., Truhlar, D. G., and Garrett, B. C. (1993) *J. Am. Chem. Soc. 115*, 7806. (b) Fernandez-Ramos, A., and Truhlar, D. G. (2001) *J. Chem. Phys. 114*, 1491.
47. Brooks, B. R., Bruccoleri, R. E., Olafson, B. D., States, D. J., and Swaminathan, S. (1983) *J. Comput. Chem. 4*, 187.
48. (a) MacKerell, A., Bashford, D., Bellot, M., Dunbrack, R., Evanseck, J. D., Field, M., Gao, J., Guo, H., Ha, S., Joseph, D., Kuchnir, L., Kuczera, K., Lau, F., Mattos, C., Minchnick, S., Ngo, T., Nguyen, D., Prodhom, B., Reiher, W. E., Roux, B., Schlenkrich, M., Smith, J., Stote, R., Strub, J., Watanabe, M., Wiokiewicz-Kuczera, J., Yin, D., and Karplus, M. (1998) *J. Phys. Chem. B 102*, 3586. (b) Pavelites, J. J. P., Gao, J., Bash, P. A., and MacKerell, A. D., Jr. (1997) *J. Comput. Chem. 18*, 221.
49. Jorgensen, W. L., Chandrasekhar, J., Madura, J. D., Impey, R. W., and Klein, M. L. (1983) *J. Chem. Phys. 79*, 926.
50. Mulliken, R. S. (1955) *J. Chem. Phys. 23*, 1833.
51. Dewar, M. J. S., Zoebisch, E. G., Healy, E. F., and Stewart, J. J. P. (1985) *J. Am. Chem. Soc. 107*, 3902.
52. Stewart, J. J. P. (1989) *J. Comput. Chem. 10*, 221.
53. Adamo, C., and Barone, V. (1997) *Chem. Phys. Lett. 274*, 242.
54. Lynch, B. J., Zhao, Y., and Truhlar, D. G. (2003) *J. Phys. Chem. A 107*, 1384.
55. Hockney, R. W. (1970) *Methods Comput. Phys. 9*, 136−211.
56. Nosé, S. (1984) *J. Chem. Phys. 81*, 511.
57. Hoover, W. G. (1985) *Phys. Rev. A 31*, 1695.
58. Andersen, H. C. (1980) *J. Chem. Phys. 72*, 2384.
59. Rychaert, J. P., Cicotti, G., and Berensden, H. J. C. (1977) *J. Comput. Phys. 23*, 327.
60. Shirley, W. A., and Brooks, C. L., III. (1997) *Proteins: Struct. Funct. Genet. 28*, 59.
61. Verlet, L. (1967) *Phys. Rev. 159*, 98.
62. Kumar, S., Bouzida, D., Swendsen, R. H., Kollman, P. A., and Rosenberg, J. M. (1992) *J. Comput. Chem. 13*, 1011.
63. Boczko, E. M., and Brooks, C. L., III. (1993) *J. Phys. Chem. 97*, 4509.
64. Rajamani, R., Naidoo, K., and Gao, J. (2003) *J. Comput. Chem.*, in press.
65. Alhambra, C., Gao, J., Corchado, J. C., Villa, J., and Truhlar, D. G. (1999) *J. Am. Chem. Soc. 121*, 2253.
66. Alhambra, C., Corchado, J. C., Sánchez, M. L., Villà, J., Gao, J., Truhlar, D. G. CHARMMRATE-version 1.0, a module of CHARMM-version 27.
67. Corchado, J. C., Chuang, Y.-Y., Fast, P. L., Vill, J., Hu, W.-P., Liu, Y.-P., Lynch, G. C., Nguyen, K. A., Jackels, C. F., Melissas, V. S., Lynch, B., Rossi, I., Coitio, E. L., Steckler, R., Garrett, B. C., Isaacson, A. D., and Truhlar, D. G. POLYRATE 8.5b, University of Minnesota, Minneapolis, MN, 1999.
68. Alhambra, C., Sanchez, M. L., Corchado, J., Gao, J., and Truhlar, D. G. (2002) *Chem. Phys. Lett. 355*, 388.
69. Fletcher, R. (1987) *Practical Methods of Optimization*, Wiley, New York.
70. Press, W. H., Flannery, B. P., Teukolsky, S. A., and Vetterling, W. T. (1986) *Numerical Recipies*, Cambridge University Press, Cambridge.
71. Garrett, B. C., Redmon, M. J., Steckler, R., Truhlar, D. G., Baldridge, K. K., Bartol, D., Schmidt, M. W., and Gordon, M. S. (1988) *J. Phys. Chem. 92*, 1476.
72. Wu, Y.-D., and Houk, K. N. (1987) *J. Am. Chem. Soc. 109*, 906.
73. Andres, J., Safont, V. S., Martins, J. B. L., Beltran, A., and Moliner, V. (1995) *J. Mol. Struct. 330*, 411.
74. Rickert, K. W., and Klinman, J. P. (1999) *Biochemistry 38*, 12218. Brazeau, B. J., Wallar, B. J., and Lipscomb, J. D. (2001) *J. Am. Chem. Soc. 123*, 10421. Rubach, J. K., Ramaswamy, S., and Plapp, B. V. (2001) *Biochemistry 40*, 12686. Knapp, M. J., Rickert, K., and Klinman, J. P. (2002) *J. Am. Chem. Soc. 124*, 3865. Hothi, P., Basran, J., Sutcliff, M. J., and Scrutton, N. S. (2003) *Biochemistry 42*, 3966. Segraves, E. N., and Holman, T. R. (2003) *Biochemistry 42*, 5236.
75. Billeter, S. R., Webb, S. P., Iordanov, T., Agawal, P. K., and Hammes-Schiffer, S. (2001) *J. Chem. Phys. 114*, 6925.
76. Hammes-Schiffer, S. (2001) *Int. Rev. Phys. Chem. 20*, 591.
77. Billeter, S. R., Webb, S. P., Agarwal, P. K., Iordanov, T., and Hammes-Schiffer, S. (2001) *J. Am. Chem. Soc. 123*, 11262.
78. Nicoll, R. M., Hindle, S. A., MacKenzie, G., Hillier, I. H., and Burton, N. A. (2001) *Theor. Chem. Acc. 106*, 105.
79. Faulder, P. F., Tresadern, G., Chohan, K. K., Scrutton, N. S., Sutcliffe, M. J., Hillier, I. H., and Burton, N. A. (2001) *J. Am. Chem. Soc. 123*, 8604.
80. Garcia-Viloca, M., Alhambra, C., Truhlar, D. G., and Gao, J. (2002) *J. Am. Chem. Soc. 124*, 7268.
81. Cui, Q., Elstner, M., and Karplus, M. (2002) *J. Am. Chem. Soc. 106*, 2721. Cui, Q., and Karplus, M. (2002) *J. Am. Chem. Soc. 124*, 3093.

82. Tresadern, G., McNamara, J. P., Mohr, M., Wang, H., Burton, N. A., and Hillier, I. H. (2002) *Chem. Phys. Lett. 358*, 489. Tresadern, G., Nunez, S., Faulder, P. F., Wong, H., Hillier, I. H., and Burton, N. A. (2003) *Faraday Discuss. 122*, 223. Tresadern, G., Faulder P. F., Gleeson, M. P., Tai, Z., MacKenzie, G., Burton, N. A., and Hillier, I. H. (2003) *Theor. Chem. Acc. 109*, 108.
83. Sutcliffe, M. J., and Scrutton, N. S. (2002) *Eur. J. Biochem. 269*, 3096.
84. Li, L., Wright, P. E., Benkovic, S. J., and Falzone, C. J. (1992) *Biochemistry 31*, 7826.
85. Lavie, A., Allen, K.-N., Petsko, G. A., and Ringe, D. (1994) *Biochemistry 33*, 5469.
86. McMillan, F. M., Cahoon, M., White, A., Hedstrom, L., Petsko, G. A., and Ringe, D. (2000) *Biochemistry 39*, 4533.
87. Stroud, R. M., and Finer-Moore, J. S. (2003) *Biochemistry 42*, 239.
88. Yu, E. W., and Koshland, D. E., Jr. (2001) *Proc. Natl. Acad. Sci. U.S.A. 98*, 9517.
89. Gao, J. (2003) *Curr. Opin. Struct. Biol. 13*, 184.
90. Bash, P. A., Field, M. J., Davenport, R. C., Petsko, G. A., Ringe, D., and Karplus, M. (1991) *Biochemistry 30*, 5826.
91. Cui, Q., and Karplus, M. (2001) *J. Am. Chem. Soc. 123*, 2284.
92. Gao, J., Kuczera, K., Tidor, B., and Karplus, M. (1989) *Science 244*, 1069.
93. Zhu, X.-Q., Liu, Y., Zhao, B.-J., and Cheng, J.-P. (2001) *J. Org. Chem. 66*, 370.
94. Marcus, R. A. (1963) *Annu. Rev. Phys. Chem. 15*, 155.
95. Zusman, L. D. (1980) *Chem. Phys. 49*, 295.
96. Hynes, J. T. (1985) in *Theory of Chemical Reaction Dynamics* (Baer, M., Ed.) Vol. 4, p 171, CRC Press, Boca Raton.
97. Hwang, J.-K., King, G., Creighton, S., and Warshel, A. (1988) *J. Am. Chem. Soc. 110*, 5297.
98. Warshel, A. (1991) *Computer Modeling of Chemical Reactions in Enzymes and Solutions*, Wiley, New York.
99. Yadav, A., Jackson, R. M., Holbrook, J. J., and Warshel, A. (1991) *J. Am. Chem. Soc. 113*, 4800.
100. Muller, R. P., and Warshel, A. (1995) *J. Phys. Chem. 99*, 17516.
101. Zhou, H.-X., and Szabo, A. (1995) *J. Chem. Phys. 103*, 3481.
102. Ando, K., and Hynes, J. T. (1997) *J. Phys. Chem. B 101*, 104564.
103. Mo, Y., and Gao, J. (2000) *J. Phys. Chem. A 104*, 3012.
104. Villa, J., and Warshel, A. (2001) *J. Phys. Chem. B 105*, 7887.
105. Schenter, G. K., Garrett, B. C., and Truhlar, D. G. (2001) *J. Phys. Chem. B 105*, 9672.
106. van Gunsteren, W. F., Billeter, S. R., Eising, A. A., Hünenberger, P. H., Krüger, P., Mark, A. E., Scott, W. R. P., and Tironi, I. G. *Biomolecular Simulation: The GROMOS96 Manual and User Guide*; Biomos b.v., Zürich and Groningen, VdF Hochschulverlag, ETH Zürich: Zürich, 1996.
107. Warshel, A., and Bentzien, J. (1999) *ACS Symp. Ser. 721*, 489.

BI034824F